



Mantle Degassing Lifetimes through Galactic Time and the Maximum Age Stagnant-lid Rocky Exoplanets Can Support Temperate Climates

Cayman T. Unterborn¹ , Bradford J. Foley² , Steven J. Desch³ , Patrick A. Young³ , Gregory Vance³, Lee Chiffelle³, and Stephen R. Kane⁴

¹ Southwest Research Institute, San Antonio, TX 78238, USA; cayman.unterborn@swri.org

² Department of Geosciences, Pennsylvania State University, University Park, PA 16802, USA

³ School of Earth and Space Exploration, Arizona State University, Tempe, AZ 85004, USA

⁴ Department of Earth and Planetary Sciences, University of California, Riverside, CA 92521, USA

Received 2022 February 14; revised 2022 April 6; accepted 2022 April 8; published 2022 May 3

Abstract

The ideal exoplanets to search for life are those within a star’s habitable zone. However, even within the habitable zone, planets can still develop uninhabitable climate states. Sustaining a temperate climate over geologic (\sim gigayear) timescales requires a planet to contain sufficient internal energy to power a planetary-scale carbon cycle. A major component of a rocky planet’s energy budget is the heat produced by the decay of radioactive elements, especially ^{40}K , ^{232}Th , ^{235}U , and ^{238}U . As the planet ages and these elements decay, this radiogenic energy source dwindles. Here we estimate the probability distribution of the amount of these heat-producing elements that enter into rocky exoplanets through Galactic history by combining the system-to-system variation seen in stellar abundance data with the results from Galactic chemical evolution models. From this, we perform Monte Carlo thermal evolution models that maximize the mantle cooling rate, thus allowing us to create a pessimistic estimate of lifetime a rocky, stagnant-lid exoplanet can support a global carbon cycle through Galactic history. We apply this framework to a sample of 17 likely rocky exoplanets with measured ages, seven of which we predict are likely to be actively degassing today, despite our pessimistic assumptions. For the remaining planets, including those orbiting TRAPPIST-1, we cannot confidently assume that they currently contain sufficient internal heat to support mantle degassing at a rate sufficient to sustain a global carbon cycle or temperate climate without additional tidal heating or undergoing plate tectonics.

Unified Astronomy Thesaurus concepts: [Exoplanet evolution \(491\)](#); [Exoplanet astronomy \(486\)](#)

1. Introduction

The climate state of an exoplanet is a primary determining factor of whether it is likely to be habitable as we know it. While life may manifest within subglacial oceans, such as those on icy moons, surface life is more easily detected remotely. Thus, a temperate surface is often considered a first-order requirement for detectable life to develop on a planet. The likelihood of a temperate climate is typically assessed based on the stellar radiation a planet receives, particularly whether it lies within its host star’s so-called “habitable zone” (e.g., Kasting et al. 1993; Kopparapu et al. 2013). Lying within a star’s habitable zone, however, does not guarantee that a planet will have a temperate surface suitable for liquid water or life. Indeed, to truly be considered habitable, a planet must be neither too hot to evaporate the entirety of its water or sterilize the planet’s surface (e.g., Abbot et al. 2012; Foley & Driscoll 2016) nor too cold to undergo global glaciation (Kadoya & Tajika 2014; Menou 2015; Haqq-Misra et al. 2016); both extremes can develop even within the nominal habitable zone.

Whether a planet is capable of consistently remaining in this temperate state over geologic (\sim gigayear) timescales relies, in part, on its ability to regulate the abundance of greenhouse gases in its atmosphere. Of the major greenhouse gases, CO_2 is known to be regulated by the carbonate-silicate cycle, at least

on Earth. The balance between the rate of delivery of CO_2 to the atmosphere via melt-induced degassing of carbon in the mantle or crust, weathering, and return of C in the form of carbonates to the mantle determines atmospheric CO_2 concentrations; negative feedback involved in surface weathering and degassing helps to stabilize climate (e.g., Walker et al. 1981; Sleep & Zahnle 2001; Kasting & Catling 2003; Foley & Driscoll 2016). However, this stabilizing feedback can fail if the input rate of CO_2 to the atmosphere from degassing drops too low, as weathering can draw down atmospheric CO_2 levels low enough for the planet to potentially fall into a snowball climate state. A planet without active degassing will lack an active carbonate-silicate cycle and the stabilizing climate feedback it provides. Specifically, a lack of degassing is likely to lead to frozen snowball climates on most habitable zone planets (Foley & Smye 2018; Foley 2019), except for planets with large C budgets, where hothouse climates are likely to form instead (Foley & Smye 2018; Foley 2019). While temperate climates may be possible on water worlds without active mantle degassing (Kite & Ford 2018), it is not known whether this extends to more Earth-like planets, with Earth-like levels of surface volatiles.

How long planets can maintain mantle degassing is a critical determinate in whether a planet is potentially habitable today, when we observe it. The age of an exoplanet is roughly the age of its host star. If the host star is older than the degassing lifetime of the planet in question, it is possible that the planet is unable to sustain the feedback necessary for climate regulation. Mantle degassing is ultimately caused by the surface-to-interior interplay between mantle volcanism and surface tectonic

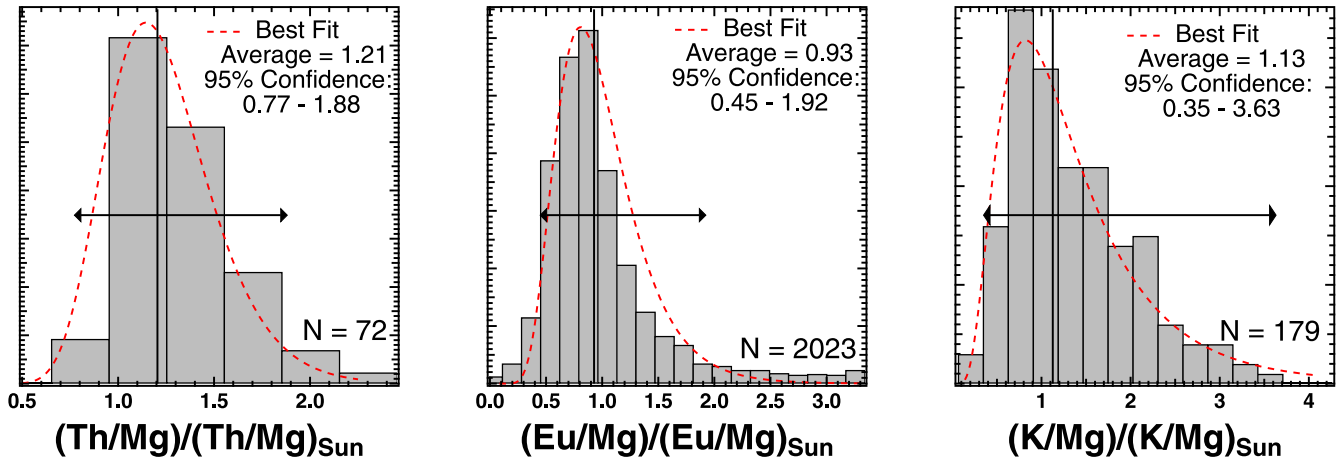


Figure 1. Histograms of measured abundances of Th (left), Eu (as a proxy for U; middle), and K (right) for our samples of stars described in Appendix A.4. The total number of stars in each sample is noted. Best fits assuming a lognormal distribution are shown in red, with the average value and 95% confidence interval shown for each element in each panel.

processes, both of which are powered by the internal heat budget of the planet (Foley & Smye 2018; Foley 2019). As a planet ages, it cools as its heat budget decreases over time. Planetary heat budgets are composed of a variety of sources: secular cooling after planet formation, the gravitational potential energy released during core and mantle differentiation, the crystallization of any inner core, tidal heating induced by the host star or other planets in the system, and the radioactive decay of the long-lived radionuclides ^{235}U , ^{238}U , ^{232}Th , and ^{40}K . In all, these elements account for ~ 100 TW, or 30%–50%, of the Earth’s current surface heat flow. Due to the radioactive nature of these elements, however, this current heat flow represents only $\sim 20\%$ of the Earth’s radiogenic heat budget when it formed ~ 4.5 Gyr ago.

Planetary radiogenic heat budgets are dependent only on the total abundances of the heat-producing elements (HPEs) U, Th, and K within their interior. Like all elements present in a planet, radionuclide concentrations are set by the abundance of these elements in the protoplanetary nebula, and their subsequent fractionation is relative to the primary rocky-planet elements (Mg, Si, Fe) during planet formation and the final distribution of these elements between the exoplanet mantle, core, and crust. Unterborn et al. (2015) proposed that the concentration of Th in an exoplanet’s host star can provide a rough estimate for the Th concentration in an orbiting rocky planet’s mantle due to its long half-life and refractory nature. Unterborn et al. (2015) and Botelho et al. (2019) observed over a factor of 2 variation in Th relative to the Sun in a sample of solar twins. Furthermore, the Hypatia catalog (Hinkel et al. 2014) shows significant variation in the abundances of Th, bulk K, and bulk U, the latter inferred from its nucleosynthetic proxy Eu, suggesting that there may be significant system-to-system variation in the abundances of the HPEs (Figure 1), meaning some exoplanets may form with a higher or lower concentration of HPEs than the Earth and Sun. Previous work has highlighted the importance of HPEs for the longevity of potentially habitable climates on stagnant-lid planets and planets with plate tectonics (Foley & Smye 2018; Foley 2019; Nimmo et al. 2020; Oosterloo et al. 2021). These previous studies, however, treated HPE abundance as a free parameter, rather than constrained by observations of the HPEs themselves (Foley & Smye 2018; Foley 2019; Nimmo et al. 2020;

Oosterloo et al. 2021). In this work, we quantify the degree of variation in each of the HPEs through Galactic history and explore the effects of this range of radiogenic heat budgets on the lifetime of mantle degassing.

2. Estimating Mantle Degassing Lifetime

To estimate the lifetime of mantle degassing, we utilize an updated version of the thermal evolution models of Foley & Smye (2018) and Foley (2019; Appendices A.1 and A.2). We define the lifetime of mantle degassing as the planet’s age when its degassing rate first falls below 10% of the Earth’s present-day degassing rate ($\approx 6 \times 10^2$ mol yr $^{-1}$; Marty & Tolstikhin 1998), scaled linearly by planet surface area (see Appendix A). Below this 10% threshold, CO_2 -poor snowball climates are expected to form, as at these low degassing rates, a steady state between weathering and degassing results in CO_2 levels too low to prevent global glaciation (Kadoya & Tajika 2014; Haqq-Misra et al. 2016; Foley 2019). To estimate the range of planetary degassing lifetimes, we adopt a Monte Carlo approach, randomly sampling within the best-fit distributions from Figure 1 to determine a planet’s initial budget of Th, U (as Eu), and K, accounting for the volatility in each element during planet formation and applying corrections for the production and decay of the HPEs through time from Galactic chemical evolution (GCE) models (Frank et al. 2014; Appendices A.3 and A.4). Additionally, we randomly sample within uniform distributions of mantle reference viscosities and initial temperatures, both key geophysical parameters that affect a planet’s thermal history (Table A1, Appendix A.5). For a given planet mass between 1 and 6 M_{\oplus} and planet formation times, t , between the birth of the Milky Way ($t = 0$ Gyr) and today ($t = 12.5$ Gyr), we perform $\sim 10^5$ thermal evolution models using these randomly determined values as inputs. Individual thermal evolution models are then run until the degassing rate falls below 10% of the Earth’s current value.

We focus our modeling on stagnant-lid exoplanets. Stagnant-lid tectonics may be the most likely dynamic state for rocky exoplanets, as the Earth is the only rocky planet we know of that exhibits plate tectonics (e.g., Breuer & Moore 2015) and the special conditions thought to be needed for platelike mantle convection to develop (e.g., Bercovici et al. 2015). While plate

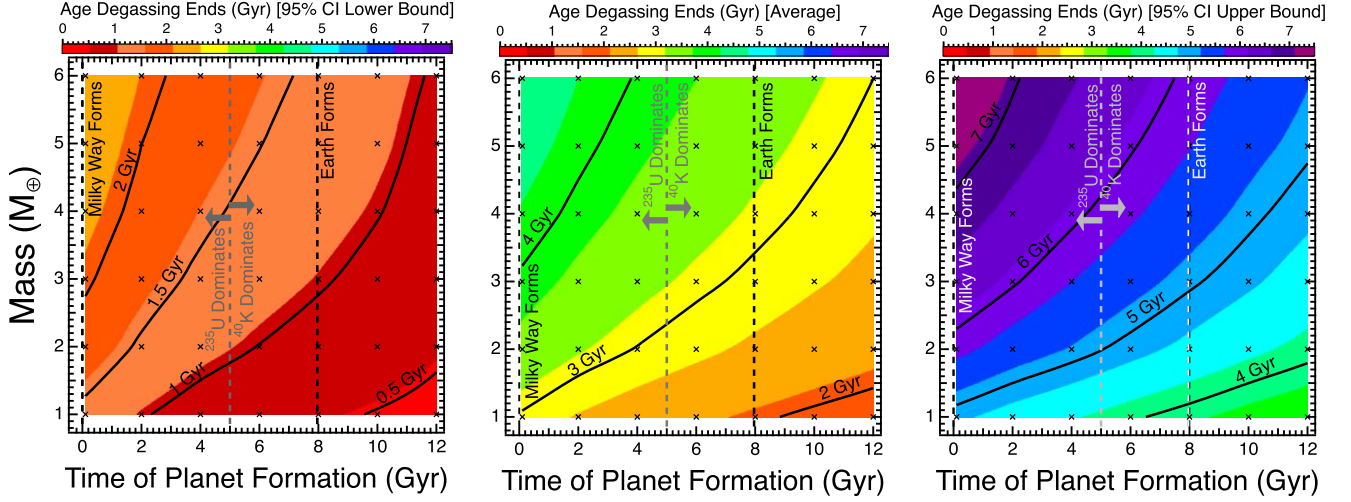


Figure 2. Interpolated color maps of average (middle), lower (left), and upper (right) 95% confidence interval bounds on the mantle degassing lifetime for stagnant-lid exoplanets as a function of planet mass and age of the system. The data interpolated are represented by crosses with averages and confidence intervals being determined by 50,000 random samplings of our parameter space (see Appendix A). We define the cessation of degassing as occurring when the degassing rate drops below 10% of the Earth’s current value, scaled linearly by planet surface area (see Appendix A).

tectonics has many advantages over stagnant-lid tectonics when it comes to mantle degassing (e.g., Foley & Driscoll 2016; Nimmo et al. 2020), whether a planet is in the plate tectonic or stagnant-lid regime is highly uncertain and difficult to predict from first principles (e.g., O’Neill & Lenardic 2007; Valencia et al. 2007; van Heck & Tackley 2011; Foley et al. 2012; Noack & Breuer 2014). Critically, however, by assuming a stagnant-lid state of tectonics, our thermal evolution models make pessimistic assumptions regarding the mantle cooling rate. Specifically, we assume that all melt produced contributes to mantle cooling by the release of latent heat and cooling of the hot melt at the planet’s surface. This implicitly assumes that all melt produced is erupted, when in reality, up to 90% of melt may intrude and solidify at depth (Crisp 1984). We also ignore heating from the cooling of the core and thus assume planets with mantles that are entirely internally heated. The effect is to produce the fastest reasonable mantle cooling rate. That is, our models will produce the shortest reasonable degassing lifetime for the rocky planets modeled. The pessimistic nature of our models means that our most robust predictions are for planets that could still be degassing today; relaxing assumptions in our models would only act to increase the degassing lifetime. This means that those planets we estimate could be degassing with stagnant lids would be even more likely to be degassing today if they instead experience plate tectonics.

For a stagnant-lid rocky exoplanet, we find that the lifetime of mantle degassing increases with planet mass but has decreased as the Galaxy has aged (Figure 2). We find that this lifetime is primarily a function of a planet’s initial radiogenic heat budget, Q_0 , and the reference mantle viscosity, with little dependence on the initial mantle temperature or the planet’s central Fe-core mass fraction (Figures A2 and A3), similar to Foley & Smye (2018). With higher Q_0 , the planet has more heating power and can thus stay warm enough to melt and degas for longer. As the Galaxy aged, the individual HPEs were produced and decayed at different rates, meaning the concentration a planet would inherit upon its formation and Q_0 are both a function of when it formed in Galactic history

(Appendix B.1; Figure A1; Frank et al. 2014). We also find that a higher reference viscosity slows mantle cooling, thereby allowing high temperatures and therefore a greater degree of volcanism, thus allowing mantle degassing to be sustained for longer (Figure A2). A larger reference viscosity also makes the stagnant lid thicker, which reduces the rate of mantle melting and hence outgassing. However, this latter effect is less important than the effect of greater retention of interior heat.

From these degassing lifetimes, we estimate the distribution of the maximum current ages, Age_{max} , for which a stagnant-lid exoplanet will be actively degassing today ($t = 12.5$ Gyr; Figure A5). Because of the pessimistic assumptions adopted in our model, planets younger than Age_{max} very likely contain sufficient radiogenic heat to be degassing today, regardless of their tectonic state. Planets older than Age_{max} , however, would require additional compositional or geophysical complexity to be included in our model, some of which we explore below. Adopting the average degassing lifetime for a given mass and formation time, we estimate an average maximum age, $\text{Age}_{\text{max}}^{\text{Avg}}$, for planets between 1 and $6 M_{\oplus}$ to be

$$\text{Age}_{\text{max}}^{\text{Avg}} = -7.1 + 8.9 \left(\frac{M_p}{M_{\oplus}} \right)^{0.09} \text{ Gyr}. \quad (1)$$

This equation incorporates the effects of GCE on HPE abundance and the potential system-to-system variation in HPE concentration based on stellar abundance measurements (Figures A1 and 1), reference viscosity, and initial mantle temperature. From this equation, we estimate the average maximum age, $\text{Age}_{\text{max}}^{\text{Avg}}$, to be ~ 1.8 Gyr for $1 M_{\oplus}$ stagnant-lid exoplanets, increasing to ~ 3.3 Gyr for $6 M_{\oplus}$ planets (Figure A5, middle).

Using the upper limit of the 95% confidence interval of our predicted degassing lifetimes for a given mass and formation time (Figure A5, right), we estimate the upper limit of the 95% confidence interval in the maximum age, $\text{Age}_{\text{max}}^{\text{UL95\%CI}}$, for

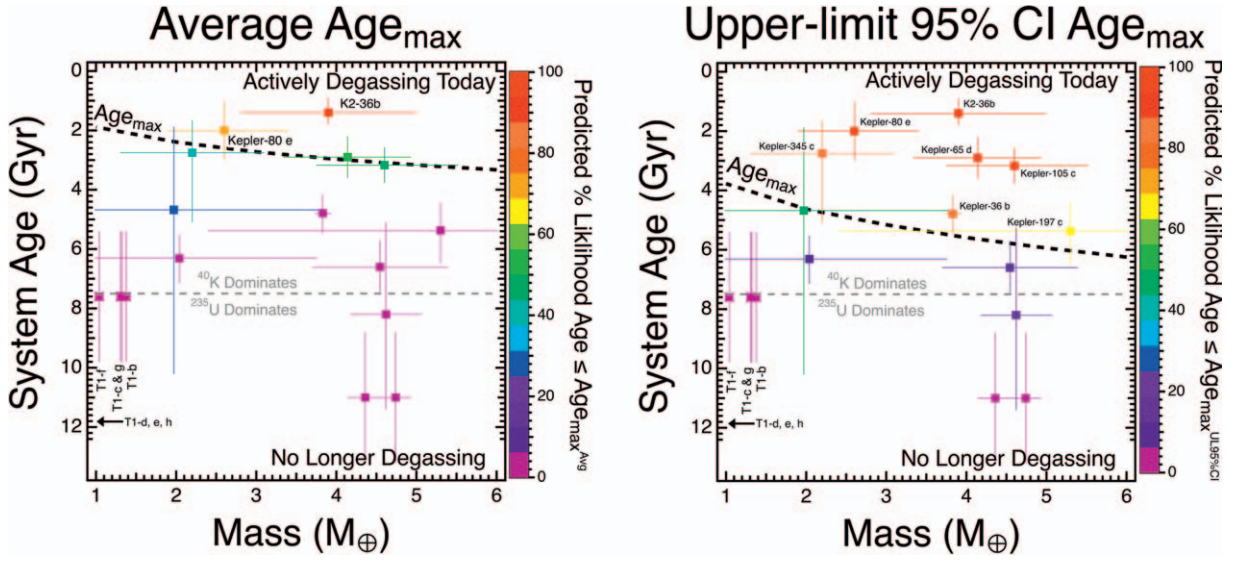


Figure 3. Probability that the host-star/planet age is $\leq \text{Age}_{\text{max}}^{\text{Avg}}$ (left) and $\leq \text{Age}_{\text{max}}^{\text{UL95\%CI}}$ (right) for the 17 planets in our sample (Table A2) as a function of their mass and system age. Planets with probabilities greater than 1σ (67%) confidence are labeled, and TRAPPIST-1 is included for reference. We define active degassing as having degassing rates greater than 10% of the Earth’s current value, scaled linearly by planet surface area (see Appendix A).

planets between 1 and $6 M_{\oplus}$ to be

$$\text{Age}_{\text{max}}^{\text{UL95\%CI}} = -1.7 + 5.4 \left(\frac{M_p}{M_{\oplus}} \right)^{0.21} \text{ Gyr}. \quad (2)$$

This yields $\text{Age}_{\text{max}}^{\text{UL95\%CI}}$ values of ~ 3.7 and 6.2 Gyr for 1 and $6 M_{\oplus}$ planets, respectively (Figure A5, right). These longer degassing lifetimes are primarily only relevant for planets with reference viscosities 10–100 times that of the Earth (Figure A4). Conversely, at the lower limit of the 95% confidence interval of our predicted degassing lifetimes, $1 M_{\oplus}$ planets would only be degassing today if younger than ~ 500 Myr, with this maximum age increasing to 1 Gyr for $6 M_{\oplus}$ planets (Figure A5, left).

Of all exoplanets discovered to date, 694 have reported measurements of mass, radius, and host-star age, as well as the respective uncertainties in each, according to the NASA exoplanet archive (Akeson et al. 2013; 10.26133/NEA1). Of these, we find 17 planets (Table A2) between 1 and $6 M_{\oplus}$ with average bulk densities $> 5 \text{ g cm}^{-3}$, a density high enough to maximize the likelihood that these planets are rocky without significant H_2/He atmospheres (Schulze et al. 2021) and equilibrium surface temperatures below the zero-pressure melting curve of dry peridotite (~ 1300 K; Katz et al. 2003), thus allowing a solid surface. These planets represent a range of ages between 1.4 and 11 Gyr. Assuming that a planet’s mass and age form a bivariate normal distribution, we estimate the probability that these likely rocky exoplanets are younger than Age_{max} for their mass and thus the likelihood that they are actively degassing today. Because of the dependence of the degassing lifetime on the planet’s HPE budget and mantle reference viscosity (Figures A2, A4, A6 and A7), and the lack of empirical constraints on mantle viscosity, we calculate Age_{max} using the average degassing lifetime from Figure 2 (middle; $\text{Age}_{\text{max}}^{\text{Avg}}$) and the upper bound of the 95% confidence interval (Figure 2, right; $\text{Age}_{\text{max}}^{\text{UL95\%CI}}$), which represents our least pessimistic estimate of Age_{max} .

We estimate that only one planet, K2-36b, is younger than $\text{Age}_{\text{max}}^{\text{Avg}}$ for its mass at greater than 2σ (95%) confidence (Figure 3; Table A2). Additionally, at the 1σ ($>67\%$) confidence level, Kepler-80 e is younger than $\text{Age}_{\text{max}}^{\text{Avg}}$. These planets would still require a sufficient HPE abundance to support degassing lifetimes longer than their current age, but there is no requirement for high mantle reference viscosity $\gtrsim 10^{23}$ Pa s (Figures A4, A6, and A7). Adopting the more optimistic $\text{Age}_{\text{max}}^{\text{UL95\%CI}}$, three additional planets are younger than this maximum age for their mass at $\geq 2\sigma$ confidence (Kepler-80 e, Kepler-65 d, and Kepler-105 c) and two at $>1\sigma$ confidence (Kepler-245 c and Kepler-36 b). We note, though, that the stagnant-lid exoplanets younger than $\text{Age}_{\text{max}}^{\text{UL95\%CI}}$ would require both a sufficient HPE budget and mantle reference viscosities 10–100 times greater than the Earth’s based on our pessimistic thermal evolution models (Figures A4, A6, and A7).

The remaining 10 planets in this sample all have probabilities below $\sim 50\%$ of being younger than $\text{Age}_{\text{max}}^{\text{UL95\%CI}}$, including the TRAPPIST-1 system. We therefore cannot confidently assume that these planets are actively degassing at a sufficient rate to sustain a temperate climate today. Our model, however, is intentionally pessimistic in its determination of Age_{max} . There are a number of factors, aside from the radiogenic HPE budget and planet size, that can change a planet’s degassing lifetime that are not included in our model. By examining the effects of these additional parameters on our model results, we can gauge the degree to which Age_{max} can change as we relax the pessimistic assumptions of our model.

3. Factors that Extend Stagnant-lid Degassing Lifetimes

Of the HPEs, ^{40}K is the dominant element controlling the lifetime of mantle degassing (Figures A6 and A7) and thus sets Age_{max} for those planets likely degassing today. Unlike Th and U, a planet’s concentrations of K and ^{40}K are not directly inferable from abundance determinations of the host star (Appendix B.2). The ^{40}K is a moderately volatile element, meaning its concentration relative to the rock-building elements

(e.g., Mg) in a planet will be reduced compared to the host star due to volatilization effects during planet formation. Furthermore, the host star only reveals information on the bulk K abundance, and not the $^{40}\text{K}/\text{K}$ ratio; whether the Earth's initial $^{40}\text{K}/\text{K}$ ratio of 0.1419% is universal for all rocky exoplanets is unknown. We estimate that simply doubling $^{40}\text{K}/\text{K}$ would increase the distribution of Age_{max} by ~ 1 Gyr (Figure B1). An effective method for altering a planet's $^{40}\text{K}/\text{K}$ is supernova injection of ^{40}K -rich material into the protoplanetary disk prior to planet formation. Little work, however, has been done to estimate the range of possible exoplanetary $^{40}\text{K}/\text{K}$ via this process. We therefore modeled the production and distribution of ^{40}K and K in a $15 M_{\odot}$ supernova progenitor (Appendix B.2, Figures B2 and B3). We find that while the production of extremely ^{40}K -rich material is possible, the total mass injected into the disk is unlikely to increase a protoplanet's $^{40}\text{K}/\text{K}$ by any appreciable amount, except potentially for those orbiting in low-mass, M dwarf disks.

Mantle reference viscosity is the other key factor controlling the degassing lifetime and Age_{max} . On average, we find that the degassing lifetime increases by ~ 0.66 Gyr per factor of 10 increase in reference viscosity for a $1 M_{\oplus}$ planet and ~ 0.92 Gyr for a $6 M_{\oplus}$ planet. These would then correspond to increases in $\text{Age}_{\text{max}}^{\text{Avg}}$ of ~ 0.71 and ~ 1.03 Gyr per factor of 10 increase in mantle reference viscosity, respectively. Because viscosity increases with pressure (e.g., Karato & Wu 1993; Hirth & Kohlstedt 2003), super-Earth lower mantles can have very large viscosities (e.g., Stamenkovic et al. 2011; Tackley et al. 2013; Noack & Breuer 2014; Schaefer & Sasselov 2015) due to their larger core–mantle boundary pressure (Unterborn & Panero 2019). As a result, mantle reference viscosity may, on average, increase with increasing planet size, leading to a corresponding increase in $\text{Age}_{\text{max}}^{\text{Avg}}$, such that $\text{Age}_{\text{max}}^{\text{Avg}}$ may increase more sharply with planet size than our model results indicate. However, viscosity extrapolations to such extreme temperature–pressure conditions are highly uncertain (Karato 2011). Moreover, if the increase in viscosity with depth is large enough, the lower mantles of super-Earths may cease convecting entirely.

Dorn et al. (2018) found that planets larger than $3\text{--}4 M_{\oplus}$ may not experience outgassing at all due to melt forming at a high enough pressure that it would be too dense to rise to the surface. In contrast, our models find that melt forms at low enough pressures to be buoyant regardless of planet size, unless the reference viscosity is increased to $\sim 10^{24}\text{--}10^{25}$ Pa s, a factor of $\sim 10\text{--}100$ above the upper bound in our models. Testing this very high viscosity case, we find that volcanism and degassing are precluded on planets larger than $>2\text{--}3 M_{\oplus}$, consistent with Dorn et al. (2018). A further increase in reference viscosity would prevent volcanism from ever occurring on planets of all sizes. Determining the exact cause of the difference between our results and Dorn et al. (2018) would require a detailed study with numerical convection models and is therefore beyond this paper's scope. However, it is likely related to the inclusion of pressure-dependent viscosity in Dorn et al. (2018); this causes higher viscosity in the lower mantle as the planet size increases, potentially leading to overall less vigorous convection and thicker lithospheres that suppress melting. Mantle viscosity is therefore important in determining whether degassing is prevented on large planets due to dense melt. An additional implication of our finding on the role of mantle viscosity is that it would be difficult to extend degassing

lifetimes, or Age_{max} , much beyond our 95% confidence interval upper limit by increasing mantle viscosity, especially for larger planets; these high viscosities would instead prevent degassing entirely.

The reference viscosity is also influenced by planet composition, including both the relative abundances of the major rock-forming elements (Mg, Si, Fe) and the oxidation state of these elements. Fayalite (Fe_2SiO_4) has a lower viscosity by a factor of ~ 1000 than forsterite (Mg_2SiO_4 and the dominant component of Earth's mantle), meaning a more FeO-rich mantle will have a lower viscosity than a Mg-rich one (Zhao et al. 2009), likely lowering Age_{max} . Mantle FeO content, however, also decreases the melting temperature of the mantle, making melting and degassing easier. More in-depth models are needed to analyze these counteracting effects. Viscosity will also depend on silica (SiO_2) content, with a lower Mg/Si leading to a higher viscosity (Ballmer et al. 2017; Spaargaren et al. 2020). However, the effect is limited, as even a very silica-rich planet with Mg/Si = 0.5 only has a factor of ~ 10 higher viscosity than the Earth (Spaargaren et al. 2020). Silica-rich planets may therefore have a slightly higher distribution of Age_{max} than those with an Earth-like planet composition considered in our model. Studies of stellar abundances, however, predict that mantles with such a low mantle Mg/Si due to silica enrichment are very rare (Unterborn & Panero 2019; Spaargaren et al. 2020).

Finally, mantle volatile content, in particular water, is known from rock deformation experiments to have a significant effect on viscosity (e.g., Hirth & Kohlstedt 1996), with the viscosity of the mantle rock decreasing with increasing water content. At the same time, water content also affects the mantle solidus, with melting temperatures decreasing as mantle water content increases (e.g., Kushiro et al. 1968). These two effects counteract each other. The same is true for other compositional factors, such as mantle Fe content (Dorn et al. 2018). Ultimately, to fully capture these competing effects, new models incorporating the combined compositional effects on viscosity and solidus would be needed. However, we provide a first-order estimate of how Age_{max} changes with mantle water content based on model suites where the mantle solidus and reference viscosity are systematically varied using the solidus parameterization of Katz et al. (2003) and the diffusion creep viscosity flow laws of Hirth & Kohlstedt (2003; Appendix B.4).

For water contents $\gtrsim 0.05\text{--}0.1$ wt%, the effect of water lowering mantle viscosities dominates, causing $\text{Age}_{\text{max}}^{\text{Avg}}$ to decrease compared to a dry-planet baseline, as the lower viscosity leads to more rapid cooling (Figure B5). Above these water contents, the decrease in solidus temperature begins to dominate, and $\text{Age}_{\text{max}}^{\text{Avg}}$ begins to increase in comparison to a dry-planet baseline, as mantle melting can occur at lower temperatures. For a $1 M_{\oplus}$ planet, we find that $\text{Age}_{\text{max}}^{\text{Avg}}$ can be lowered by at most ~ 1.4 Gyr for moderate water contents ($\sim 0.05\text{--}0.1$ wt%) and raised by up to ~ 1.6 Gyr for higher water contents (~ 0.3 wt%), with the exact change depending on the chosen water viscosity dependency exponent, r (Figure B5). These effects are more pronounced for a $6 M_{\oplus}$ planet. These estimates are likely upper limits, as we do not include the overburden pressure of surface water, which will lower the rate of, or entirely prevent, volcanism (Kite et al. 2009; Cowan & Abbot 2014; Krissansen-Totton et al. 2021), as well as the evolution of the in- and outgassing rates of water

over time (e.g., McGovern & Schubert 1989; Crowley et al. 2011; Spaargaren et al. 2020).

The addition of tidal (e.g., Barnes et al. 2009; Driscoll & Barnes 2015) or magnetic induction (e.g., Kislyakova et al. 2017) heating would also prolong mantle degassing and increase Age_{max} beyond our model estimates. Both of these sources of heat depend on a planet’s orbit and will persist as long as the orbital configuration allows, unlike radiogenic heat sources, which decay over time. Planets heated by tides or magnetic induction can therefore sustain degassing for very long times, potentially even indefinitely. Exoplanetary orbit parameters can be constrained observationally, so the likelihood of significant tidal or magnetic induction heating can be estimated in most cases.

As explained above, our model makes pessimistic assumptions that err on the side of hastening the end of volcanism, including neglecting mantle plumes and assuming all melt erupts at the surface. We found that varying melt intrusion did not significantly change our results; 90% melt intrusion increases our estimated degassing lifetime by only ~ 100 Myr for an Earth-mass planet. Mantle plumes, however, can prolong volcanism, even after the upper mantle has cooled below the point where it can melt through passive upwelling, depending on the temperature difference between the plume and surrounding mantle. While the effect of plumes can only be fully captured with higher-dimensional dynamic models, we can roughly approximate how much they might extend the degassing lifetime based on our models, where the mantle solidus temperature was varied (Figure B4). There we found that a 100°C decrease in solidus temperature increases the degassing lifetime by ≈ 0.4 Gyr for a $1 M_\oplus$ planet. Therefore, if the upwelling plumes are 100°C – 300°C hotter than the surrounding mantle, as estimated for Earth (White & McKenzie 1995; Shen et al. 1998; Thompson & Gibson 2000), degassing could last up to ≈ 0.4 – 1.2 Gyr longer. If plume volcanism is as active as Earth, it likely could maintain sufficient CO_2 outgassing for maintaining a temperate climate, as plume volcanism accounts for \approx one-third of the CO_2 degassing on Earth (Marty & Tolstikhin 1998). Plume activity may be more muted on stagnant-lid planets, however, as inefficient mantle cooling leads to a smaller temperature anomaly for plumes (O’Rourke & Korenaga 2015), so the estimates given here for how plumes prolong volcanism should be considered upper bounds.

Our model predictions can also be applied to Venus, assuming it is a stagnant-lid planet. Venus is a $0.82 M_\oplus$ planet, meaning that our model predicts average and upper-limit Age_{max} values of 1.6 and 3.5 Gyr, respectively. That is, it should not exhibit significant enough volcanism and outgassing today to support a temperate climate ($>10\%$ of Earth’s present rate). There is some evidence, however, for volcanism and outgassing in the last <1 Myr (Smrekar et al. 2010; Filiberto et al. 2020; Byrne & Krishnamoorthy 2022), likely plume-related (Gülcher et al. 2020). If corroborated, this would not necessarily invalidate the model predictions, as the rates of Venusian volcanism are probably too low to support outgassing rates above our threshold rate of degassing to support a temperate climate. Estimates of the rate of volcanism on Venus, if present, are uncertain, but most fall in the range of ~ 0.1 – $1 \text{ km}^3 \text{ yr}^{-1}$, with a highest estimate of $\sim 10 \text{ km}^3 \text{ yr}^{-1}$ (Fegley & Prinn 1989; Byrne & Krishnamoorthy 2022, and references therein). These volcanism rates are therefore ~ 30 – 300 times

lower (with a minimum of two times lower for the highest rate for Venus) than Earth’s estimated 26 – $34 \text{ km}^3 \text{ yr}^{-1}$ (Crisp 1984) and would lead to comparably lower CO_2 outgassing rates. Only the upper-end estimate of $\sim 10 \text{ km}^3 \text{ yr}^{-1}$ would be large enough to drive CO_2 outgassing at a rate $>10\%$ of the modern Earth’s. Moreover, it is possible that Venus is experiencing volcanism due to lying in a tectonic regime intermediate to stagnant-lid and plate tectonic end-members and therefore having a thinner lithosphere than expected for a purely stagnant-lid planet. There is evidence for limited plate tectonics-like subduction (Sandwell & Schubert 1992; Davaille et al. 2017) and the relative movement of crustal blocks on the surface (Byrne et al. 2021), as well a relatively thin lithosphere and high heat flux, compared to pure stagnant-lid models (Borrelli et al. 2021). Venus, therefore, demonstrates that planets may operate in a regime intermediate to the end-member plate tectonics and stagnant-lid regimes, leading to longer-lived volcanism than our pessimistic stagnant-lid models predict.

Plate tectonics can drastically increase the lifetime of degassing on a rocky exoplanet to ages beyond Age_{max} due to lithospheric thinning allowing for mantle material to melt at lower temperatures (e.g., Kite et al. 2009). For planets significantly older than Age_{max} , where tidal or induction heating is unlikely, our stagnant-lid framework would not be able to explain any atmospheric observations showing atmospheric chemistries indicative of active mantle degassing or the presence of a temperate climate. These older planets, then, may provide an ideal sample to search for rocky exoplanets undergoing plate tectonics similar to Earth or indicate planets with complex tectonic histories that have potentially transitioned between different tectonic modes over time.

Our definition of Age_{max} represents a pessimistic upper limit of the “temporal habitable zone” for rocky, stagnant-lid exoplanets not undergoing tidal heating. For planets older than this zone, we estimate that they will have exhausted their internal radiogenic heat budget to the point where interior melting is limited and mantle degassing rates are no longer sufficient to support a temperate climate today, when we observe it. Other compositional and dynamical factors may increase Age_{max} for these stagnant-lid planets, as described above; however, they are often fraught with other complications that may impact other aspects of planetary habitability.

4. Conclusion

An individual rocky exoplanet provides us with a sparseness of direct data with which to understand its evolution. Host-star age and radionuclide abundance, while indirectly telling us about the planet, are critical, and currently underutilized, observables that will allow us to better understand both an exoplanet’s history and its current likelihood of being temperate today, regardless of tectonic state. The framework we present here that combines direct and indirect observational data with dynamical models not only provides us with a pessimistic baseline for understanding which parameter(s) most control a stagnant-lid exoplanet’s ability to support a temperate climate but also indicates where more lab-based and computational work is needed to quantify the reasonable range of these parameters (e.g., mantle reference viscosity). As we move to more in-depth characterization of individual targets in the James Webb Space Telescope era, these direct and indirect astronomic observables, coupled with laboratory data and

models from the geoscience community, will allow us to better estimate whether a rocky exoplanet in both the canonical and temporal habitable zones has exhausted its internal heat and is simply too old to be Earth-like.

C.T.U. acknowledges the support of Arizona State University through the SESE Exploration fellowship. The results reported herein benefited from collaborations and/or information exchange within NASA’s Nexus for Exoplanet System Science (NExSS) research coordination network, sponsored by NASA’s Science Mission Directorate. The authors gratefully acknowledge support from grant NNX15AD53G awarded to S.D. We thank the anonymous reviewer for helpful comments that improved the manuscript’s clarity considerably.

Appendix A Methods

We adopt the stagnant-lid thermal evolution model of Foley & Smye (2018) and Foley (2019), updated to account for a planet’s mass, core mass fraction (CMF), metamorphic degassing rate, individual HPE contents, fractionation of HPEs into the crust, and solidus changes due to mantle depletion (Sections A.1 and A.2). In these models, the initial radioactive heat production budgets are determined in a Monte Carlo sampling within the observed variability of HPEs in FGK stars, corrected for fractionation and volatility effects (Appendix A.3). We define the cessation of degassing as the moment when a planet’s degassing rate first falls below 10% of the Earth’s present-day degassing rate ($\approx 6 \times 10^{12}$ mol yr⁻¹; Marty & Tolstikhin 1998), scaled linearly by planet surface area. Foley (2019) confirmed that degassing rates must be >10% of the modern-day Earth’s for a temperate climate on stagnant-lid planets, even if the planet is mostly ocean-covered and thus dominated by seafloor weathering. Seafloor weathering has an overall slower rate than continental weathering on the modern Earth; thus, with only seafloor weathering, active atmospheric CO₂ levels (and surface temperatures) would be higher for a given degassing rate (e.g., Krissansen-Totton & Catling 2017; Glaser et al. 2020; Hayworth & Foley 2020). Planets with higher land fractions would thus require higher degassing rates than our chosen threshold to remain temperate. Moreover, our degassing rate threshold was determined for a planet receiving a stellar radiative flux equal to what Earth receives today. Lower incoming radiative fluxes would also require higher rates of degassing than our assumed threshold in order to sustain temperate climates.

We scale our degassing rate threshold with planet surface area because the total weathering rate increases linearly with the area of weatherable rock. Thus, a planet with a larger surface area will need a proportionally higher degassing rate to sustain a temperate climate. Ultimately, planets with degassing rates below our threshold for temperate climates may not be the best targets for atmospheric characterization or detectable surface life, as they are likely to lie in snowball climate states. Finally, another climate extreme is possible if the rate of CO₂ degassing overwhelms the surface weathering rate; this will produce a hothouse, Venus-like climate.

A.1. Updates to Thermal Evolution Model

Foley & Smye (2018) and Foley (2019) gave a thorough description of our model, and all of the key governing

Table A1
Range and Sampled Distribution Type for Monte Carlo Models

Parameter	Sampled Range	Distribution Type
K/Mg/(K/Mg) _⊙	Avg: 1.38; 95% CI: 0.37–3.67	Lognormal distribution
Th/Mg/(Th/Mg) _⊙	Avg: 1.24; 95% CI: 0.77–1.88	Lognormal distribution
U/Mg/(U/Mg) _⊙	Avg: 0.99; 95% CI: 0.45–1.92	Lognormal distribution
Mantle reference viscosity	10 ¹⁹ –10 ²³ Pa s	Flat distribution
Initial mantle temperature	1700–2000 K	Flat distribution

equations are listed in Appendix A.2. Here we will only highlight the differences between the model of Foley & Smye (2018) and the model presented in this paper. For an Earth-like CMF = 0.33, we use the scaling laws from Valencia et al. (2006, 2007) to determine the average mantle density, planet radius, mantle thickness, and surface gravity as a function of planet mass:

$$\rho = \rho_{\oplus} \left(\frac{M_p}{M_{\oplus}} \right)^{0.2}, \quad (\text{A1})$$

$$R_p = R_{\oplus} \left(\frac{M_p}{M_{\oplus}} \right)^{0.27}, \quad (\text{A2})$$

$$d = d_{\oplus} \left(\frac{M_p}{M_{\oplus}} \right)^{0.28}, \quad (\text{A3})$$

$$g = \frac{GM_p}{R_p^2}, \quad (\text{A4})$$

where M_p is the planet mass, and G is the gravitational constant. Reference Earth values are $\rho_{\oplus} = 4450$ kg m⁻³, $R_{\oplus} = 6378$ km, and $d_{\oplus} = 2890$ km.

To vary the CMF, we use the scaling laws from Noack et al. (2016; see also Foley et al. 2020), which assume that all iron resides in the core. The resulting equations for R_p , R_c , and ρ , as a function of CMF and planet mass, are

$$R_p = (7121 - 2021 \times \text{CMF}) \left(\frac{M_p}{M_{\oplus}} \right)^{0.265} \text{ km}, \quad (\text{A5})$$

$$R_c = (19200 \times \text{CMF} - 31760 \times \text{CMF}^2 + 18100 \times \text{CMF}^3) \left(\frac{M_p}{M_{\oplus}} \right)^{0.252} \text{ km}, \quad (\text{A6})$$

$$\rho = \frac{(1 - \text{CMF})M_p}{\frac{4}{3}\pi(R_p^3 - R_c^3)}. \quad (\text{A7})$$

Gravity is still calculated from Equation (A4).

We assume that all other material properties are independent of planet size and CMF. This is a simplification because thermal conductivity, expansivity, and viscosity are all functions of pressure, and the larger the planet or core, the higher the pressures reached in the mantle. However, robust parameterizations for how to incorporate these pressure effects are currently lacking. There is still significant uncertainty about how key material properties change at the extreme temperature and pressure conditions of super-Earth lower mantles, which are not yet experimentally accessible (e.g., Duffy et al. 2015).

Table A2
Sample of Likely Solid Rocky Planets

Planet	Mass (M_{\oplus})	Density (g cm^{-3})	Age (Gyr)	T_{eq} (K)	% Probability Age \leq Age $_{\text{max}}^{\text{Avg}}$	% Probability Age \leq Age $_{\text{max}}^{\text{UL95\%CI}}$
K2-36 b	3.9 \pm 1.1	7.3 \pm 2.1	1.4 \pm 0.45	1224	100	100
Kepler-80 e	2.6 \pm 0.75	6.5 \pm 1.9	2 \pm 1	629	70	99
Kepler-65 d	4.14 \pm 0.8	6.5 \pm 1.2	2.9 \pm 0.7	1117	56	100
Kepler-138 c	1.97 \pm 1.5	6.3 \pm 4.9	4.68 \pm 4.17	402	26	44
Kepler-105 c	4.6 \pm 0.9	11.2 \pm 2.2	3.17 \pm 0.6	997	45	100
Kepler-345 c	2.2 \pm 0.9	7.0 \pm 2.9	2.75 \pm 1.7	575	42	83
Kepler-197 c	5.3 \pm 3.1	15.6 \pm 9.2	5.37 \pm 3.1	930	2	63
TRAPPIST-1 b	1.374 \pm 0.07	5.4 \pm 0.3	7.6 \pm 2.2	401	1	5
TRAPPIST-1 g	1.321 \pm 0.038	5.0 \pm 0.1	7.6 \pm 2.2	199	1	5
TRAPPIST-1 c	1.308 \pm 0.056	5.4 \pm 0.1	7.6 \pm 2.2	341	1	5
TRAPPIST-1 f	1.039 \pm 0.031	5.0 \pm 0.1	7.6 \pm 2.2	219	0	4
Kepler-36 b	3.83 \pm 0.1	6.3 \pm 0.2	4.79 \pm 0.65	978	0	85
HD 219134 b	4.74 \pm 0.19	6.3 \pm 0.03	11 \pm 2.2	1015	0	1
HD 219134 c	4.36 \pm 0.22	6.9 \pm 0.4	11 \pm 2.2	782	0	1
Kepler 93 b	4.54 \pm 0.85	6.5 \pm 1.2	6.6 \pm 0.9	1037	0	17
Kepler-68 c	2.04 \pm 1.75	14.4 \pm 12.3	6.31 \pm 0.82	941	0	6
HD 136352 b	4.62 \pm 0.45	7.2 \pm 0.7	8.2 \pm 3.2	911	5	22

Moreover, how significant variation of key material properties with pressure, and hence depth in a super-Earth mantle, modifies the dynamics of the convecting mantle has not been extensively studied; scaling laws for convective heat flux and velocity that take these pressure effects into account have not yet been developed.

Lacking robust parameterizations for viscosity, thermal expansivity, and thermal conductivity pressure effects, we instead randomly vary the mantle reference viscosity, μ_{ref} , in our models over a range of 4 orders of magnitude. We focus on viscosity because, of the key mantle material properties, it shows the strongest dependence on pressure and mantle composition, as it can vary by orders of magnitude (e.g., Karato & Wu 1993; Hirth & Kohlstedt 2003). We use a standard Arrhenius temperature-dependent viscosity law in our models,

$$\mu_i = \mu_n \exp\left(\frac{E_v}{RT_p}\right), \quad (\text{A8})$$

where μ_i is the mantle interior viscosity, T_p is the mantle potential temperature, $E_v = 300 \text{ kJ mol}^{-1}$ (e.g., Karato & Wu 1993) is the activation energy, and R is the universal gas constant. The reference viscosity is defined at the reference temperature $T_{\text{ref}} = 1623 \text{ K}$, or approximately Earth's present-day mantle potential temperature. The constant μ_n is then adjusted in each model run to match the chosen reference viscosity. Our results therefore explicitly demonstrate how the degassing lifetime depends on the mantle reference viscosity, which itself may vary with planet size or composition.

The equations for calculating the rate of metamorphic degassing due to crustal burial from Foley & Smye (2018) are reformulated in terms of pressure, rather than depth (see Appendix A.2.3). As such, they can then be applied to planets with variable sizes and CMFs and hence different surface gravities. Finally, we have improved the melting model to include depletion of the mantle and a subsequent increase in the melting temperature. We follow the method of Tosi et al. (2017) and assume that the solidus can increase by up to 150 K upon full depletion of the mantle, the difference in the solidi of

harzburgite and peridotite. The degree of mantle depletion is calculated based on the volume of crust present at each time step (see Appendix A.2.1). The model also tracks each of the four major HPEs separately, rather than treating them together with an average decay constant as in Foley & Smye (2018). Here we are interested in observationally constrained variations in each of the four major HPEs, so we naturally must treat each HPE separately in the model (see Appendix A.2.1). The remainder of the model equations are general and can be applied to planets with different masses and CMFs.

A.2. Thermal Evolution Model

Here we give a complete description of the coupled thermal evolution and volatile cycling model. Assuming pure internal heating, and that all melt produced contributes to the cooling of the mantle, the mantle thermal evolution is given by

$$V_{\text{man}} \rho c_p \frac{dT_p}{dt} = Q_{\text{man}} - A_{\text{man}} F_{\text{man}} - \dot{f}_m \rho_m (c_p \Delta T_m + L_m), \quad (\text{A9})$$

where V_{man} is the volume of the actively convecting mantle, ρ is the average density of the mantle, c_p is the heat capacity, T_p is the potential temperature of the mantle, t is time, Q_{man} is the total radiogenic heat production rate of the mantle, A_{man} is the surface area of the top of the convecting mantle (the base of the stagnant lid), F_{man} is the heat flux from the mantle, \dot{f}_m is the volumetric melt production rate, ρ_m is the density of melt, ΔT_m is the temperature difference between the erupted melt and the surface temperature, and L_m is the latent heat of the mantle (e.g., Stevenson et al. 1983; Hauck & Phillips 2002; Reese et al. 2007; Fraeman & Korenaga 2010; Morschhauser et al. 2011; Driscoll & Bercovici 2014; Foley & Smye 2018; Foley 2019). The volume of the convecting mantle is $V_{\text{man}} = (4/3)\pi((R_p - \delta)^3 - R_c^3)$, where R_p is the planet radius, R_c is the core radius, and δ is the thickness of the stagnant lid. The surface area of the top of the convecting mantle is then $A_{\text{man}} = 4\pi(R_p - \delta)^2$. Finally, the temperature difference between the erupted melt and the surface temperature is

$\Delta T_m = T_p - P_i \gamma - T_s$, where γ is the average adiabatic temperature gradient of the mantle melt, estimated as $\gamma \approx 2 \times 10^{-8}$ K Pa $^{-1}$ in Foley & Smye (2018), and p_i is the pressure where melting begins (derived below in Section A.2.1).

The thickness of the stagnant lid, δ , is then (e.g., Schubert et al. 1979; Spohn 1991)

$$\rho c_p (T_p - T_l) \frac{d\delta}{dt} = -F_{\text{man}} - k \frac{\partial T}{\partial z} \Big|_{z=R_p-\delta}, \quad (\text{A10})$$

where T_l is the temperature at the base of the stagnant lid, k is the thermal conductivity (assumed to be the same throughout the crust and mantle for simplicity), and z is the height above the planet's center. The mantle heat flux, F_{man} , and lid base temperature, T_l , are calculated from the following scaling laws for stagnant-lid convection (Reese et al. 1998, 1999; Solomatov & Moresi 2000; Korenaga 2009):

$$F_{\text{man}} = \frac{c_1 k (T_p - T_s)}{d} \Theta^{-4/3} Ra_i^{1/3} \quad (\text{A11})$$

and

$$T_l = T_p - \frac{a_{rh} R T_p^2}{E_v}, \quad (\text{A12})$$

where c_1 and a_{rh} are constants (assumed to be $c_1 = 0.5$ and $a_{rh} = 2.5$), and T_s is the surface temperature, here fixed to 273 K, as surface temperature fluctuations of order 100 K that could result from changes in atmospheric CO $_2$ do not significantly impact the evolution of the underlying mantle in these models (Foley 2019). The mantle thickness is $d = R_p - R_c$, and Θ is the Frank–Kamenetskii parameter, $\Theta = E_v (T_p - T_s) / (R T_p^2)$, where E_v is the activation energy for mantle viscosity, and R is the universal gas constant. The internal Rayleigh number, Ra_i , is defined as $Ra_i = \rho g \alpha (T_p - T_s) d^3 / (\kappa \mu_i)$, where g is gravity, α is the thermal expansivity of the mantle, κ is the thermal diffusivity of the mantle, and μ_i is the viscosity at the mantle potential temperature of T_p (see Equation (A8)).

A.2.1. Melting and Crustal Evolution

Large-scale mantle melting and subsequent volcanism take place when passively upwelling mantle is hot enough to cross the solidus beneath the lid. As in, e.g., Fraeman & Korenaga (2010) and Foley & Smye (2018), the pressure at which melting begins, P_i , is calculated from the intersection of the mantle adiabat, with adiabatic gradient γ_{mantle} , and the dry peridotite solidus from Takahashi & Kushiro (1983),

$$P_i = \frac{T_p - T_0^{\text{sol}}}{120 \times 10^{-9} - \gamma_{\text{mantle}}}, \quad (\text{A13})$$

where T_0^{sol} is the melting solidus temperature at zero pressure, and the adiabatic gradient in the mantle is $\gamma_{\text{mantle}} \approx 2 \times 10^{-8}$ K Pa $^{-1}$. The solidus temperature at zero pressure depends on the degree of mantle depletion, which we estimate based on the volume of crust present, as explained below. We also do not allow the pressure where melting begins to exceed 10 GPa, the approximate pressure where silicate melts become denser than solids (e.g., Dorn et al. 2018). Melting stops at the base of the

lid, which occurs at pressure

$$P_f = \rho_l g \delta, \quad (\text{A14})$$

where ρ_l is the average density of the crust and lithosphere (assumed to be $\rho_l = 3300$ kg m $^{-3}$). The melt fraction, ϕ , is

$$\phi = \frac{P_i - P_f}{2} \left(\frac{d\phi}{dP} \right)_S, \quad (\text{A15})$$

where $(d\phi/dP)_S \approx 1.5 \times 10^{-10}$ Pa $^{-1}$. The melt production rate, f_m , is calculated as (see Foley & Smye 2018 for a derivation)

$$f_m = 17.8 \pi R_p v (d_{\text{melt}} - \delta) \phi, \quad (\text{A16})$$

where v is the characteristic convecting mantle velocity and $d_{\text{melt}} = P_i / (\rho_l g)$ is the depth where melting begins. The convecting mantle velocity is (Reese et al. 1998, 1999; Solomatov & Moresi 2000; Korenaga 2009)

$$v = c_2 \frac{\kappa}{d} \left(\frac{Ra_i}{\Theta} \right)^{2/3}, \quad (\text{A17})$$

where c_2 is a constant.

Melting produces a crust whose thickness, δ_c , and volume, V_{crust} , evolve over time. To calculate the evolution of the V_{crust} , we assume that all melt produced contributes to the growth of the crust, and that all crust buried to depths below the lithospheric thickness, δ , founders into the mantle. The resulting equation is

$$\frac{dV_{\text{crust}}}{dt} = f_m - \left(f_m - 4\pi (R_p - \delta)^2 \min\left(0, \frac{d\delta}{dt}\right) \right) \times (\tanh((\delta_c - \delta)20) + 1). \quad (\text{A18})$$

The second term on the right-hand side of Equation (A18) describes the rate of crust loss due to foundering of the crust; the hyperbolic tangent function formulation allows this crust loss rate to go to zero when $\delta_c < \delta$. The term $4\pi (R_p - \delta)^2 \min(0, d\delta/dt)$ captures the loss of crust when the lid thickness is decreasing and $\delta_c = \delta$ and is zero otherwise (that is, if either the lid thickness is growing or the crust ends before the base of the stagnant lid). The crustal thickness is calculated from the volume of crust as

$$\delta_c = R_p - \left(R_p^3 - \frac{3V_{\text{crust}}}{4\pi} \right)^{1/3}. \quad (\text{A19})$$

To incorporate how depletion of the mantle influences the solidus, and thus later melt production, we increase T_0^{sol} linearly with crust thickness following (Tosi et al. 2017)

$$T_0^{\text{sol}} = 1423 + \Delta T_{\text{sol}} \times \max\left(1, \frac{\delta_c}{\delta_{\text{ref}}}\right). \quad (\text{A20})$$

Here 1423 K is the dry peridotite solidus temperature at zero pressure from Takahashi & Kushiro (1983), $\Delta T_{\text{sol}} = 150$ K is the increase in the solidus upon full depletion (which is set here to the difference in the zero-pressure solidus temperatures for peridotite and harzburgite), and $\delta_{\text{ref}} = 0.2 V_{\text{man}}^0 / A_{\text{surf}}$ is the reference crust thickness produced upon full depletion of the mantle. Here $V_{\text{man}}^0 = (4/3)\pi (R_p^3 - R_c^3)$, and $A_{\text{surf}} = 4\pi R_p^2$ is the surface area of the planet. The solidus can thus increase by up to 150 K due to mantle depletion. We explore other

compositional effects that affect the solidus (e.g., water) in the main text.

The HPEs are preferentially partitioned into the crust during mantle melting due to their incompatible nature. We track this partitioning for all four long-lived HPEs assuming accumulated fractional melting. The evolution of the crustal heat production rate for a given HPE is thus

$$\begin{aligned} \frac{dQ_{c,i}}{dt} &= \frac{x_m f_m}{\phi} [1 - (1 - \phi)^{1/D_i}] \\ &\quad - x_{c,i} \left(f_m - 4\pi(R_p - \delta)^2 \min\left(0, \frac{d\delta}{dt}\right) \right) \\ &\quad \times (\tanh((\delta_c - \delta)20) + 1) - \frac{Q_{c,i}}{\tau_i}. \end{aligned} \quad (\text{A21})$$

Here $Q_{c,i}$ is the heat production rate in the crust resulting from one of the four HPEs tracked in the model. The total crustal heat production rate $Q_{\text{crust}} = Q_{c,\text{U238}} + Q_{c,\text{U235}} + Q_{c,\text{Th}} + Q_{c,\text{K}}$. Each HPE has a specified decay constant, τ_i ; distribution coefficient, D_i ; and crustal and mantle heat production rate per unit volume, $x_{c,i}$ and $x_{m,i}$, respectively (e.g., τ_{U238} is the decay constant for ^{238}U , D_{U238} is the distribution coefficient for ^{238}U , and $x_{c,\text{U238}}$ is the heat production per unit volume in the crust due to ^{238}U). The well-known half-lives taken from Turcotte & Schubert (2002) are used to calculate the decay constants, τ_i . The chosen distribution coefficients of $D_{\text{U238}} = D_{\text{U235}} = 0.0012$ and $D_{\text{Th}} = 0.0029$ are from Beattie (1993), and $D_{\text{K}} = 0.0011$ is from Hart & Brooks (1974), assuming 60% olivine and 40% pyroxene in the mantle. The evolution of mantle heat production from a given radioactive isotope is

$$\begin{aligned} \frac{dQ_{m,i}}{dt} &= x_{c,i} \left(f_m - 4\pi(R_p - \delta)^2 \min\left(0, \frac{d\delta}{dt}\right) \right) \\ &\quad \times (\tanh((\delta_c - \delta)20) + 1) - \frac{x_m f_m}{\phi} [1 - (1 - \phi)^{1/D_i}] \\ &\quad - \frac{Q_{m,i}}{\tau_i}. \end{aligned} \quad (\text{A22})$$

As before, the total heat production rate of the mantle is $Q_{\text{man}} = Q_{m,\text{U238}} + Q_{m,\text{U235}} + Q_{m,\text{Th}} + Q_{m,\text{K}}$. The total heat production rates per unit volume in the crust and mantle are also sums of the heat production rates of the four HPEs: $x_c = x_{c,\text{U238}} + x_{c,\text{U235}} + x_{c,\text{Th}} + x_{c,\text{K}}$ and $x_m = x_{m,\text{U238}} + x_{m,\text{U235}} + x_{m,\text{Th}} + x_{m,\text{K}}$.

A.2.2. Crustal Geotherm

Equation (A10) requires as an input the conductive heat flux at the base of the lid. The temperature profile for steady-state one-dimensional heat conduction with constant heat production rates in the crust and mantle, neglecting advection, is used to determine this heat flux (for details, see Foley & Smye 2018):

$$-k \frac{\partial T}{\partial z} \Big|_{z=R_p-\delta} = \frac{k(T_l - T_c)}{\delta - \delta_c} - \frac{x_m(\delta - \delta_c)}{2} \quad (\text{A23})$$

when $\delta > \delta_c$, and

$$-k \frac{\partial T}{\partial z} \Big|_{z=R_p-\delta} = -\frac{x_c \delta_c}{2} + \frac{k(T_l - T_s)}{\delta_c} \quad (\text{A24})$$

when $\delta = \delta_c$. The temperature at the base of the crust, T_c , is

$$T_c = \frac{T_s(\delta - \delta_c) + T_l \delta_c}{\delta} + \frac{x_c \delta_c^2 (\delta - \delta_c) + x_m \delta_c (\delta - \delta_c)^2}{2k\delta}. \quad (\text{A25})$$

The mantle radiogenic heating rate per unit volume, $x_m = Q_{\text{man}}/(V_{\text{man}} + V_{\text{lid}})$, where $V_{\text{lid}} = (4/3)\pi((R_p - \delta_c)^3 - (R_p - \delta)^3)$, is the volume of the subcrustal stagnant lid. The crustal radiogenic heat rate per unit volume is $x_c = Q_{\text{crust}}/V_{\text{crust}}$, where Q_{crust} is the total radiogenic heating rate in the crust, and V_{crust} is the volume of the crust.

A.2.3. CO₂ Outgassing Rates

The CO₂ is outgassed to the atmosphere due to mantle melting, subsequent volcanism, and metamorphic breakdown of carbonated minerals as the crust is buried (Foley & Smye 2018; Foley 2019). Foley & Smye (2018) showed that the temperature as a function of depth where metamorphic decarbonation occurs can be approximated as a simple linear relationship,

$$T_{\text{decarb}} = A\rho_l g(R_p - z) + B, \quad (\text{A26})$$

where $A = 9.66 \times 10^{-8} \text{ K Pa}^{-1}$, $B = 835.5 \text{ K}$, T_{decarb} is the temperature in Kelvin, and $\rho_l = 3300 \text{ kg m}^{-3}$ is the lithosphere density. The depth where decarbonation occurs, δ_{carb} , is (for details, see Foley & Smye 2018)

$$\begin{aligned} \delta_{\text{carb}} &= \frac{\delta_c}{2} + \frac{k(T_c - T_s)}{\delta_c x_c} - \frac{A\rho_l g k}{x_c} \\ &\quad - \frac{k}{x_c} \sqrt{\left(\frac{x_c \delta_c}{2k} + \frac{T_c - T_s}{\delta_c} - A\rho_l g \right)^2 + \frac{2x_c}{k}(T_s - B)}. \end{aligned} \quad (\text{A27})$$

With the decarbonation depth determined by Equation (A27), the metamorphic outgassing flux is given by

$$F_{\text{meta}} = \frac{R_{\text{crust}} f_m}{2V_{\text{carb}}} (\tanh((\delta_c - \delta_{\text{carb}})20) + 1), \quad (\text{A28})$$

where R_{crust} is the size of the crustal CO₂ reservoir (in moles), and the hyperbolic tangent function allows F_{meta} to go to zero when $\delta_c < \delta_{\text{carb}}$ and $R_{\text{crust}} f_m / (V_{\text{carb}})$ when $\delta_c > \delta_{\text{carb}}$. The outgassing rate due to mantle melting is

$$F_d = \frac{f_m R_{\text{man}} [1 - (1 - \phi)^{1/D_{\text{CO}_2}}]}{\phi(V_{\text{man}} + V_{\text{lid}})}, \quad (\text{A29})$$

where R_{man} is the size of the mantle CO₂ reservoir, and $D_{\text{CO}_2} = 10^{-4}$ is the distribution coefficient for CO₂ (Hauri et al. 2006). The evolution of the mantle and crustal reservoirs when crustal decarbonation is active (e.g., $\delta_{\text{carb}} < \delta_c$) follows

$$\frac{dR_{\text{man}}}{dt} = -F_d, \quad (\text{A30})$$

$$\frac{dR_{\text{crust}}}{dt} = F_d, \quad (\text{A31})$$

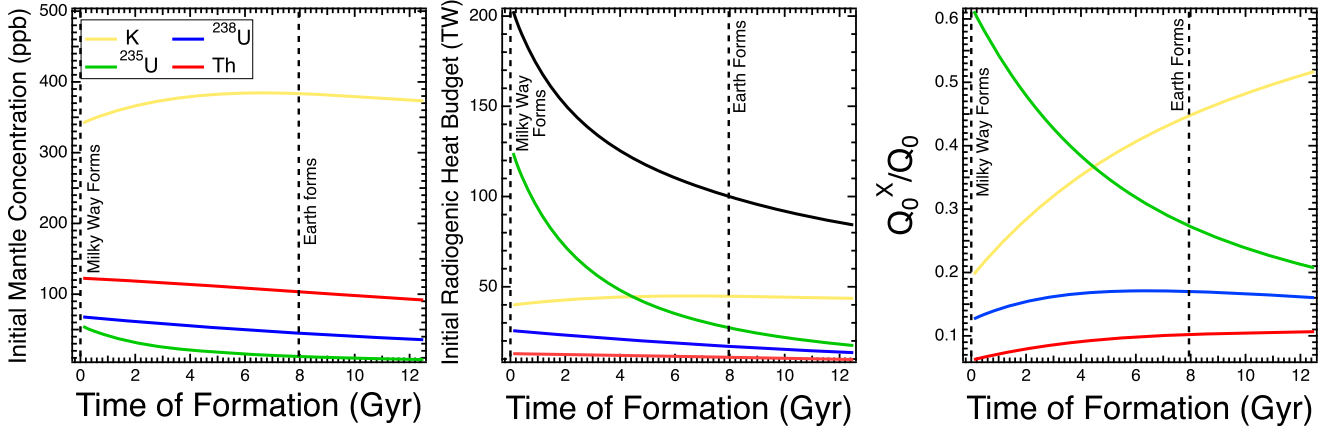


Figure A1. Initial mantle abundances (left), initial radiogenic heat budget (Q_0 ; middle), and fraction of total heat budget (right) for a cosmochemically Earth-like planet as a function of the time of planet formation from Frank et al. (2014) and adopting the current Earth HPE abundances of Palme & O’Neill (2003) for ^{40}K (yellow), ^{238}U (blue), ^{235}U (green), and Th (red). The time of Earth formation ($t = 8$ Gyr) is shown for reference.

while when crustal decarbonation is inactive ($\delta_c < \delta_{\text{carb}}$),

$$\frac{dR_{\text{crust}}}{dt} = F_d - \frac{R_{\text{crust}}}{V_{\text{crust}}} \left(f_m - 4\pi(R_p - \delta)^2 \min\left(0, \frac{d\delta}{dt}\right) \right) \times (\tanh((\delta_c - \delta)20) + 1), \quad (\text{A32})$$

$$\frac{dR_{\text{man}}}{dt} = -F_d + \frac{R_{\text{crust}}}{V_{\text{crust}}} \left(f_m - 4\pi(R_p - \delta)^2 \min\left(0, \frac{d\delta}{dt}\right) \right) \times (\tanh((\delta_c - \delta)20) + 1). \quad (\text{A33})$$

The total CO_2 budget of the mantle and crust, C_{tot} , is conserved, such that $C_{\text{tot}} = R_{\text{man}} + R_{\text{crust}}$. As in Foley & Smye (2018), the planet starts with all of the CO_2 residing in the mantle, and CO_2 is outgassed over time to the surface. The entire allotment of each HPE also initially resides in the mantle, as before planetary evolution begins, we assume that there is no crust present (crust formation does not take place until mantle convection, and subsequent volcanism, begins). The abundance of each HPE is linked to the stellar observed abundances, as explained in Appendix A.3.

Finally, an important limit for the carbon cycle and habitability is the global weathering supply limit. This limit is the upper bound on the weathering rate and set by the rate at which CO_2 drawdown will occur if all available fresh surface rock is completely carbonated as soon as it is brought to the surface. On a stagnant-lid planet, this limit is assumed to be set by volcanism. Using the average composition of basalt on Earth, the total amount of CO_2 that can be drawn down by crustal carbonation is $\chi = 5.8 \text{ mol kg}^{-1}$ of basalt (Foley 2019). We assume the crust will have a basaltic composition, as it is a result of primary mantle melting of a peridotitic mantle. Exoplanets, however, could have different mantle bulk compositions that would lead to different crustal compositions upon melting. However, the weathering demand, χ , only increases by about a factor of 2 for the extreme ultramafic composition end-member, peridotite, and only decreases by about a factor of 2 if the crust is felsic, like Earth’s continental crust. Average compositions from Taylor & McLennan (1985) for continental crust and Warren (2016) for peridotite were used in making these estimates. The total variation in weathering demand is thus approximately a factor of 4 from

ultramafic to felsic end-members. This would not significantly change the planetary conditions (e.g., mantle CO_2 budget, size, internal heat production rate, etc.) that control when planets enter a supply-limited weathering regime and thus develop hothouse climates (Foley & Smye 2018; Foley 2019).

The weathering supply limit, F_{sl} , assuming all erupted basalt is available for weathering, is

$$F_{\text{sl}} = \epsilon f_m \chi \rho_t \quad (\text{A34})$$

with units of mol yr^{-1} ; ϵ is the fraction of mantle melt produced that erupts at the surface ($\epsilon = 0.1$ is assumed). In the models, supply-limited weathering is assumed to lead to an inhospitable hothouse climate when $F_d + F_{\text{meta}} > F_{\text{sl}} + 10^{14} \text{ mol yr}^{-1}$ at any point during planetary evolution, as in Foley & Smye (2018). The total outgassing rate exceeding the weathering supply limit by $10^{14} \text{ mol yr}^{-1}$ means that hot climates, with $T_s \geq 400 \text{ K}$, would form in $\sim 100 \text{ Myr}$, well within the typical degassing lifetimes of modeled planets.

A.3. Input Radionuclide Abundances

We define the initial total heat production rate of the mantle, Q_0 , as a function of the specific power (P_X) produced by each HPE (X), their concentration within the planet (C_X), and the mass of the mantle (m_{man}). We calculate the initial HPE abundance as $Q_0 = P_X \times C_X \times m_{\text{man}}$. In order to quantify the range of HPE concentrations in rocky exoplanets (C_X^{planet}), we randomly sample within the observationally constrained stellar abundance distributions for each HPE (Figure 1 of main text) and apply the scaling relationship to convert from stellar abundance to mantle concentration as a function of planet formation time, t , after the birth of the Milky Way:

$$\frac{C_X^{\text{planet}}(t)}{C_X^{\text{Earth-like}}(t)} = \left(\frac{f_X^{\text{planet}}}{f_X^{\text{Earth}}} \right) \times \frac{C_X^{\text{star}}}{C_X^{\text{Sun}}}, \quad (\text{A35})$$

where C_X^{star} and C_X^{Sun} are the concentrations of the element in the randomly selected stellar abundance and the Sun, respectively, and f_X is a correction for volatility effects during planet formation. Here $C_X^{\text{Earth-like}}(t)$ represents the predicted initial concentration of an HPE if it was a “cosmochemically Earth-like” planet (Frank et al. 2014) forming at some t

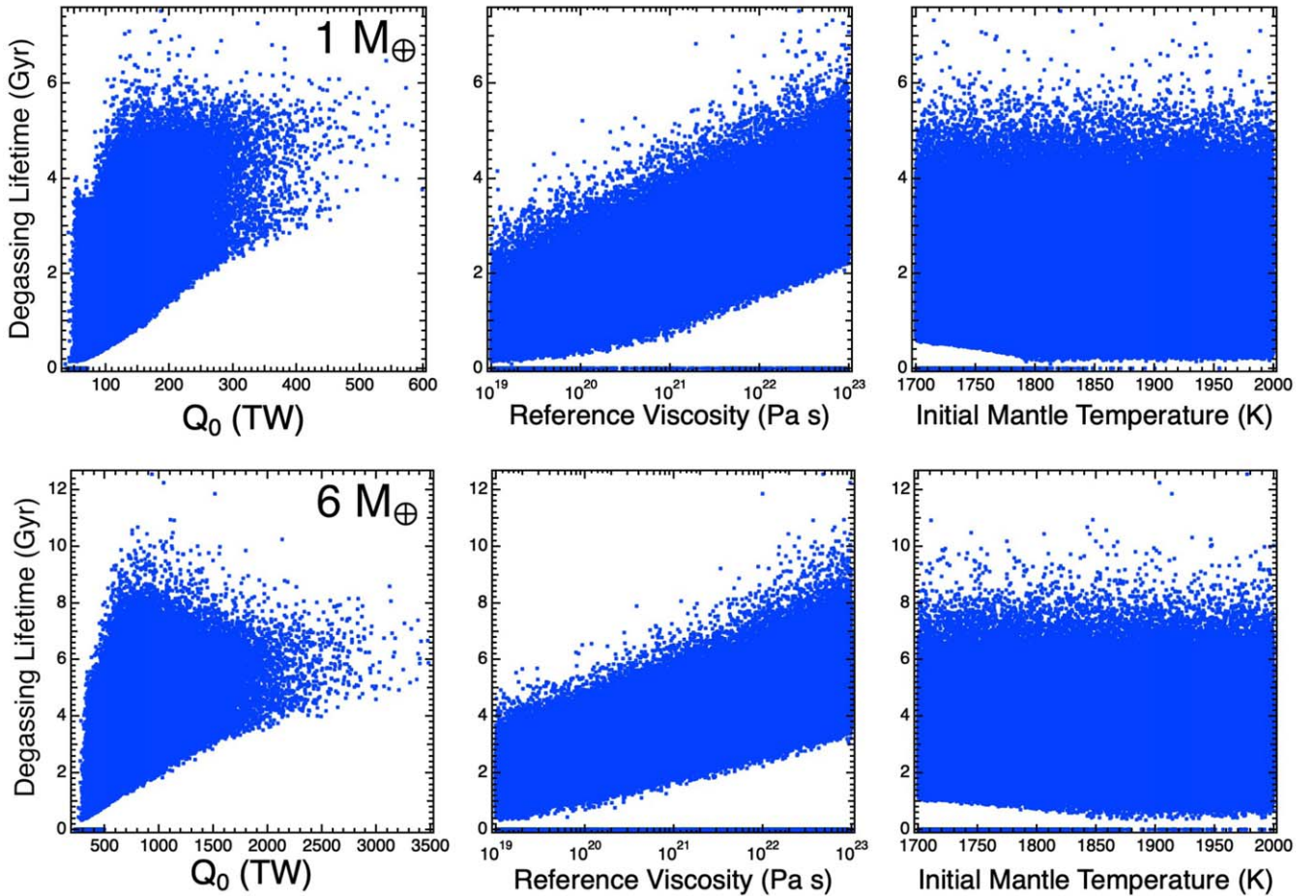


Figure A2. Degassing lifetime as a function of initial radiogenic heat budget (left), reference viscosity (middle), and initial mantle temperature (right) for 1 (top) and 6 (bottom) M_{\oplus} planets with Earth-like CMFs (0.33) that formed at the same time as the Earth ($t = 8$ Gyr).

(Figure A1). We rescale the results of Frank et al. (2014) such that the Earth-like abundance of each HPE at the time the Earth formed ($t = 8$ Gyr) is that of Palme & O’Neill (2003). This lowers our choice of $C_X^{\text{Earth-like}}$ by $\sim 25\%$ for each HPE compared to those presented in Frank et al. (2014), who adopted the initial Earth HPE abundances of Turcotte & Schubert (2002).

We define the concentration of an HPE in both stars and the Sun as its molar ratio with Mg (e.g., X/Mg). We normalize relative to Mg because it is more likely to remain in the mantle, as opposed to Si, which may partition into the core (Hirose et al. 2013). Equation (A35) then becomes

$$C_X^{\text{planet}}(t) = \left(\frac{f_X^{\text{planet}}}{f_X^{\text{Earth-like}}} \right) * \frac{(X/\text{Mg})_{\text{star}}}{(X/\text{Mg})_{\text{Sun}}} * C_X^{\text{Earth-like}}(t). \quad (\text{A36})$$

We define f_X as the fraction that an element is enriched or depleted relative to Mg during planet formation relative to the host star:

$$f_X = \frac{(X/\text{Mg})_{\text{planet}}}{(X/\text{Mg})_{\text{star}}}. \quad (\text{A37})$$

For those elements that fractionate relative to Mg during planet formation, f_X will be greater than 1 in the case of enrichment and less than 1 in the case of depletion. Of the HPEs, U and Th

are both refractory and not expected to fractionate between the star and planet relative to Mg. That is to say, f_U and f_{Th} are ~ 1 for both a rocky exoplanet and its host star, as well as the Earth and Sun. For the current bulk silicate Earth (mantle + crust), the present-day molar ratios of Th/Mg and U/Mg are 3.4×10^{-8} and 9×10^{-9} , respectively (McDonough 2003). Comparatively, the Sun’s current composition (Lodders et al. 2009), which is usually defined to be equal to the abundances in CI chondrites, has molar values of Th/Mg = 3.5×10^{-8} and U/Mg = 9.8×10^{-9} . Among all chondrites, our best proxies for planet-forming materials, their whole-rock Th/Mg and U/Mg abundance ratios, are within $<10\%$ of the CI value, except for CV chondrites, which are 1.4 times the solar value (Wasson et al. 1988). The model of Desch et al. (2018), which computes how refractory elements redistribute themselves in protoplanetary disks, predicts small deviations ($<20\%$) of the molar ratios of elements at least as refractory as Mg in planetary materials (50% condensation temperature $T_c^{\text{Mg}} = 1336$ K; Lodders 2003). The Th and U have 50% condensation temperatures of 1659 and 1610 K, respectively (Lodders 2003). Based on these models, along with chondrite abundances and the Earth’s abundances, we expect that the Th/Mg and U/Mg ratios in a rocky exoplanet should match within tens of percent of the ratios in the star. We therefore set both the Earth-like and planet values of f_{Th} and f_U to 1.

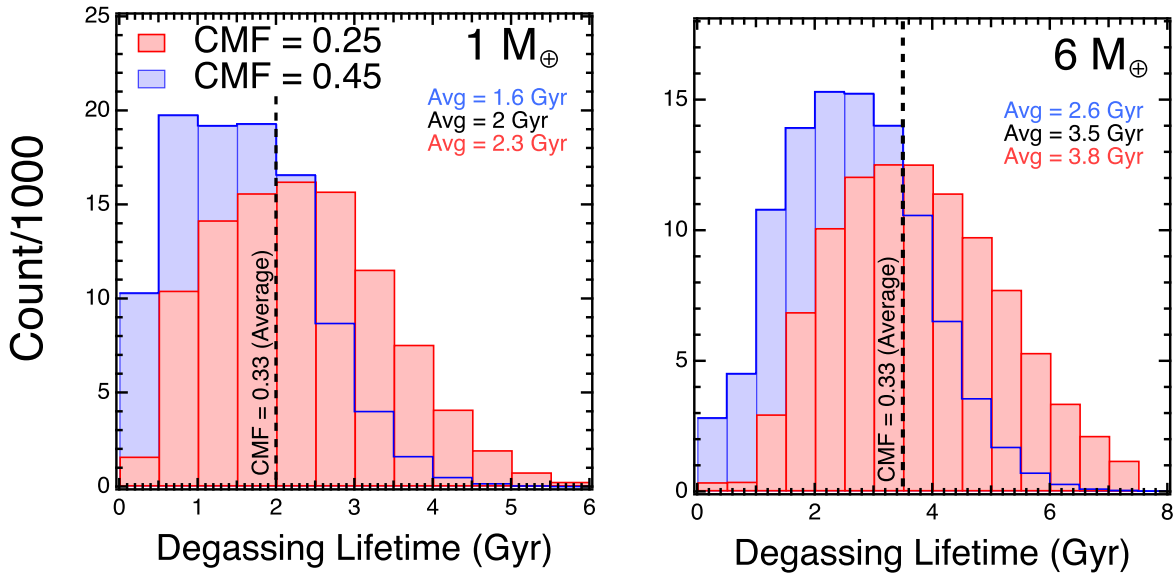


Figure A3. Histograms of the degassing lifetime for 1 (left) and 6 (right) M_{\oplus} planets with CMFs of 0.25 (red) and 0.45 (blue) for a planet forming at the same time as the Earth ($t = 8$ Gyr). The average of our CMF = 0.33 models (Figure 2 of main text) for each mass is shown as a black dashed line. These histograms were derived from 200,000 random samplings of our parameters, as described above.

In contrast to U and Th, K is substantially depleted in the Earth relative to Sun and CI chondrites, with $f_K^{\text{Earth}} = 0.19$ (McDonough 2003; Lodders et al. 2009). This is part of the well-known planetary volatility trend observed in the compositions of the Earth and other planets: elements less refractory than Mg ($T_c < T_c^{\text{Mg}}$) are depleted in the Earth, relative to Mg and CI chondrites, by amounts that increase with decreasing condensation temperature (McDonough 2003). The 50% condensation temperature of K is $T_c^K = 1006$ K (Lodders 2003), and K is thus “moderately volatile” in comparison with Mg, Th, and U. The relative volatility of K is reflected in the range of K/Mg among chondrites, which is wider than the spread in Th/Mg or U/Mg. The solar value of K/Mg is closest to the CI value of 3.6×10^{-3} ; however, it can vary from as low as 1.3×10^{-3} in CV chondrites to as high as 4.7×10^{-3} in EH chondrites and 3.2×10^{-3} in EL chondrites, i.e., from 0.4 times CI in CV to 1.3 and 0.9 times CI in EH and EL chondrites. This demonstrates that fractionation of K occurs among planetary materials, although the Earth’s depletion by a factor of 5 remains unexplained (see, however, Desch et al. 2020). Without knowledge of the mechanism that depletes K relative to Mg during planet formation, we cannot constrain f_K^{planet} . Changes in f_K^{planet} relative to f_K^{Earth} will directly change C_K^{planet} by an equal amount. Initially, we set $f_K^{\text{planet}} = f_K^{\text{Earth}} = 0.19$ and discuss the consequences of variable f_K^{planet} in the main text. The ^{40}K is not expected to fractionate relative to K in any planet formation scenario; therefore, it will be depleted by the same amount as bulk K between a star and planet.

For our models, then, C_X^{planet} is simply a function of the ratio of (X/Mg) between the star and the Sun:

$$C_X^{\text{planet}}(t) = \frac{(X/\text{Mg})_{\text{star}}}{(X/\text{Mg})_{\text{Sun}}} * C_X^{\text{Earth-like}}(t). \quad (\text{A38})$$

This method is similar to that used by Frank et al. (2014) in their determination of a cosmochemically Earth-like planet; however, our model is able to account for the system-to-system

Table A3
Model Inputs for HPEs

Element	Half-life (Gyr)	Current Earth: $t = 12.5$ Gyr Abundance (ppb) ^a	Earth: $t = 8$ Gyr Abundance (ppb)	Solar ^b X/Mg (by mol)
^{40}K	1.25	30.5	382	3.8×10^{-3c}
^{238}U	4.47	22	44	9.6×10^{-8d}
^{235}U	0.704	0.16	14	9.6×10^{-8d}
^{232}Th	14	83	104	3.5×10^{-8}

Notes.

^a Palme & O’Neill (2003).

^b Lodders et al. (2009).

^c Bulk K.

^d Bulk Eu.

variation in HPE concentrations due to inefficient mixing within the Galaxy. For all HPE concentrations relative to the Sun, we adopt the solar composition model of Lodders et al. (2009).

A.4. Observational Range of HPE Concentrations

We compile measured stellar Th abundances from Unterborn et al. (2015) and Botelho et al. (2019) for a sample of 72 solar twins and analogs (Figure 1, left). Solar twins and analogs are stars of similar metallicity (that is, iron abundance), mass, and surface temperature to the Sun. Because of these similarities to the Sun, systematic uncertainties in abundance measurements due to the assumed stellar atmosphere model are minimized, particularly of trace elements like Th. The reported Th abundances do not include abundance information for Mg, instead providing only Si. To correct for this, we assume a constant Si/Mg molar ratio equal to that of the Sun (Si/Mg = 0.95; Lodders et al. 2009) for each of these stars. The distribution of stellar Si/Mg abundances is 0.9 ± 0.2 by mole (Hinkel & Unterborn 2018); thus, the uncertainty introduced in

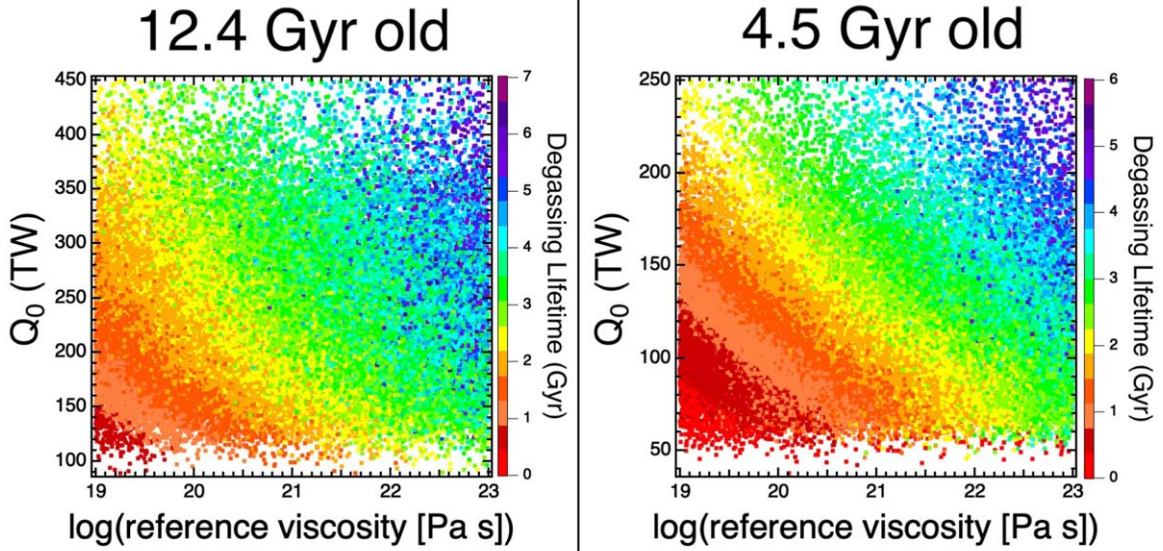


Figure A4. Age when degassing ends for $1 M_{\oplus}$ (colors) as a function of reference viscosity and the initial radiogenic heat budget for formation times 12.4 (left) and 4.5 (right) Gyr into the past. The figure was created using 50,000 random samples as described above. For comparison, the Earth’s reference viscosity is $\sim 10^{21}$ Pa s.

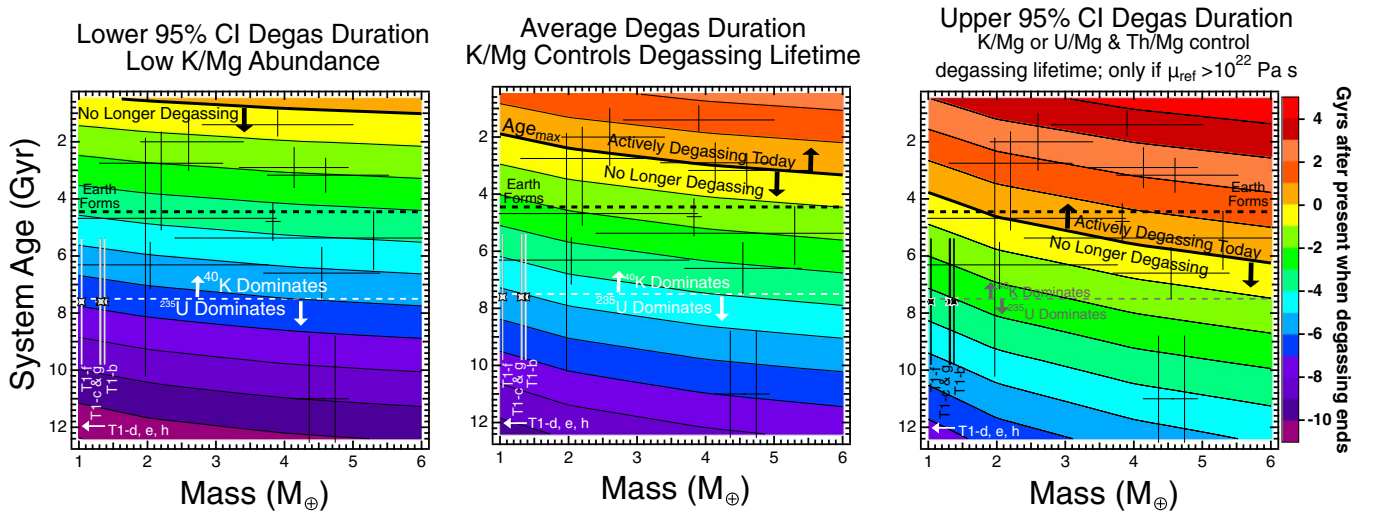


Figure A5. Planet age when degassing ceases (present = 12.5 Gyr) as a function of planetary mass and current system age adopting the average (middle) and lower (left) and upper (right) bounds of our 95% confidence intervals of degassing lifetime for planets of a given mass and time of formation (Figure 2 of main text). Those 17 planets with measured mass, radius, and system age and density consistent with being rocky are included for reference (Table A2). Uncertainties represent the reported 1σ error bars in both mass and age. The TRAPPIST-1 planets are highlighted, adopting the system ages of Burgasser & Mamajek (2017) and planet masses of Agol et al. (2021).

our conversion from Th/Si to Th/Mg does not drastically increase the range of planetary Th concentrations that we explore across our Monte Carlo thermal models. Assuming these abundances follow a lognormal distribution, we calculate an average current-day value ($t = 12.5$ Gyr after the birth of the Milky Way) of $(\text{Th}/\text{Mg})_{\text{star}} = 1.21$ times our chosen solar value (Table A3) with the 95% confidence interval between 0.77 and 1.88 times solar (Figure 1, left).

Unlike thorium, uranium has yet to be measured in young Sun-like stars. Additionally, the isotopic ratio of $^{235}\text{U}/^{238}\text{U}$ has not been measured in any system outside of the solar system. In the absence of direct observational constraints on U, we adopt Eu as its proxy. The ratios of r -process elements (i.e., Eu, Th, and U) in stars are remarkably well correlated for extremely

old, metal-poor stars with r -process enhancements (Beers & Christlieb 2005; Roederer et al. 2009; Barbuy et al. 2011; Hansen et al. 2017, and references therein). The nucleosynthetic origins of third-peak r -process elements are observationally and theoretically correlated (Goriely & Arnould 2001; Frebel et al. 2007). For the Sun, $\log(\text{U}/\text{Eu}) \approx -1$ (by mole); that is, U is depleted by a factor of 10 relative to Eu. Given that ultra- and hyper-metal-poor stars in particular may reflect element production and enrichment from single or a few events, we would expect a similarly narrow variation in both U and Eu, with little change in their abundances relative to each other due to their coproduction. The concentration of europium, defined as Eu/Mg , is then a viable proxy for predicting the system-to-system variation in U abundances. Europium is also

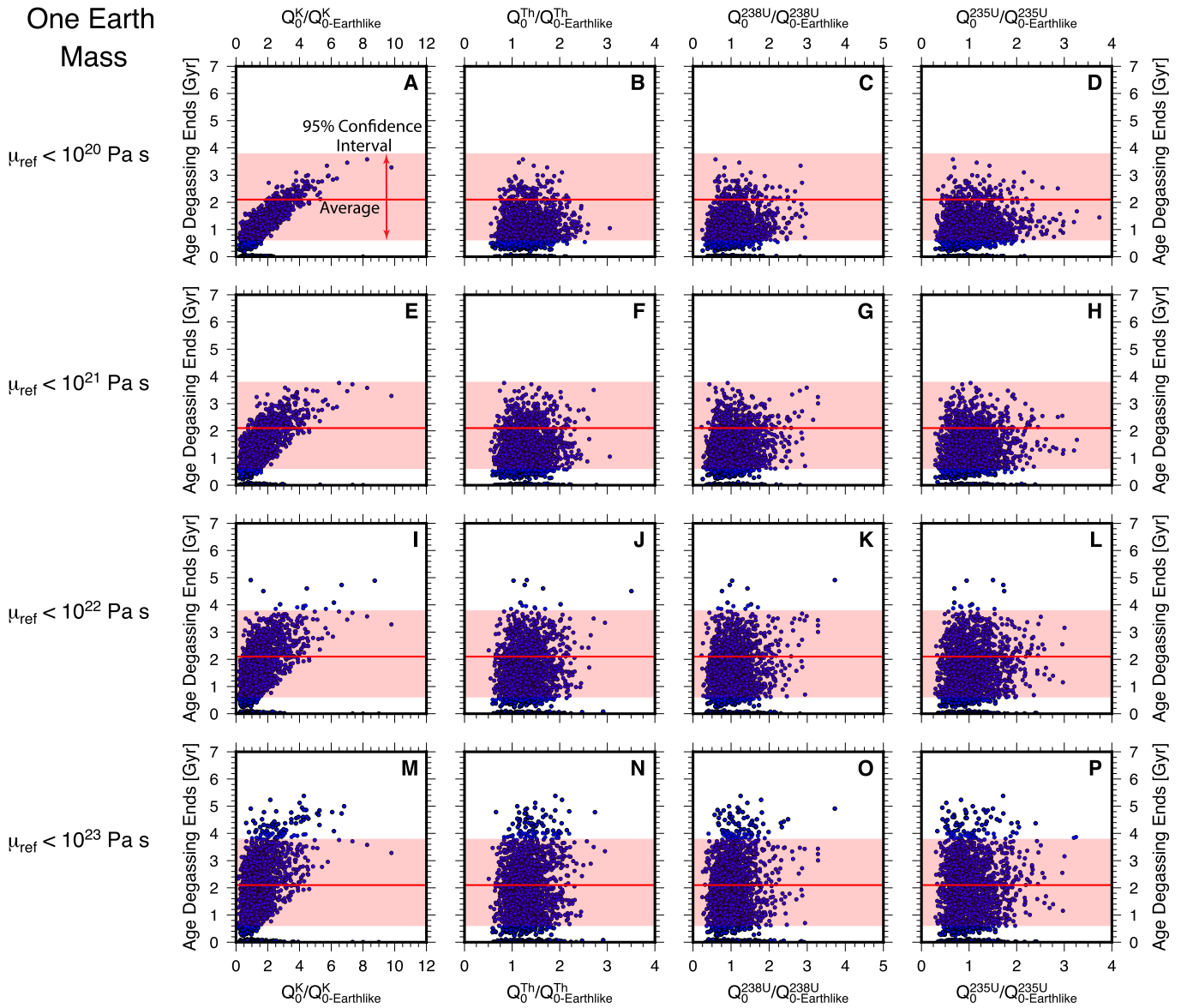


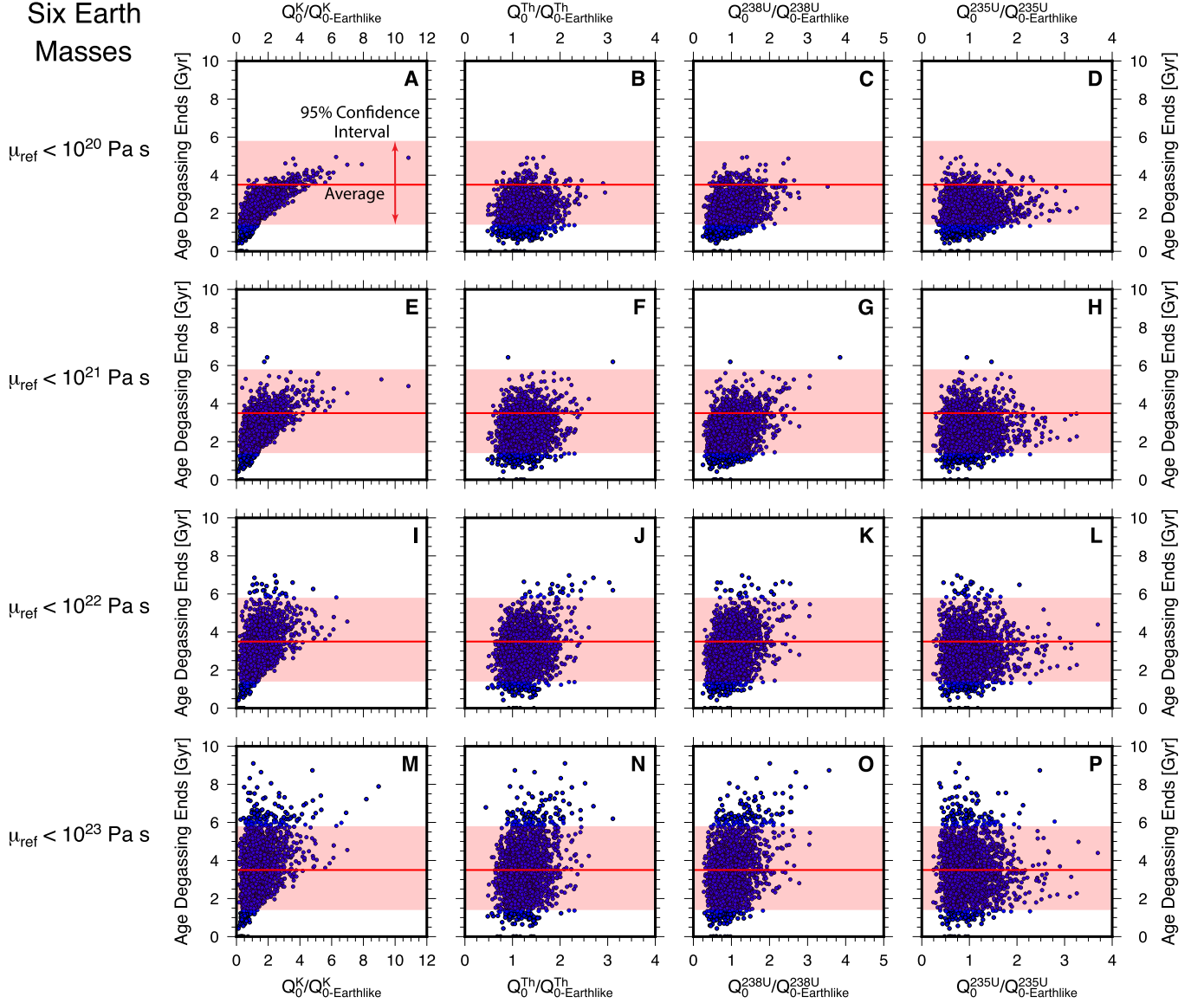
Figure A6. Age when degassing ends for a $1 M_{\oplus}$ planet as a function of the initial heat budget for an HPE $X (Q_0^X)$ relative to the initial heat budget for the same element for the Earth ($Q_0^X\text{-Earth}$; see Table A3) for restricted ranges of mantle reference viscosity: $\mu_{\text{ref}} < 10^{20}$ (first row), 10^{21} (second row), 10^{22} (third bottom row), and 10^{23} (fourth row) Pa s. Models were run assuming that planets formed at the same time as the Earth ($t = 8$ Gyr). The average (red line) and 95% confidence intervals in the degassing cessation age (red band) are included for reference. In each plot, only 2000 models are shown to reduce the density of the data points.

as refractory as U, with a 50% condensation temperature of 1356 K (Lodders 2003). Therefore, the concentration of Eu as determined from Eu/Mg is, like U, not expected to vary between host star and exoplanet by more than tens of percent, i.e., less than the total observed range. For comparison, the bulk silicate Earth has Eu/Mg by mole of 10.5×10^{-8} (McDonough 2003), while the Sun's value is nearly the same at 9.6×10^{-8} (Lodders et al. 2009). We therefore adopt Eu/Mg as a proxy for the distribution of U stellar abundances and set f_{Eu} to 1 for both the planet and Earth-like values. Both ^{235}U and ^{238}U isotope abundances are sampled independently from the Eu distribution.

Though still difficult to measure, Eu is observed in stars with reasonable frequency. We adopt a data set of 2040 FGK stars with measured Eu and Mg abundances in the Hypatia catalog (Figure 1, middle; Hinkel et al. 2014). We assume this data set to be an upper limit of the range of Eu abundances relative to

the Sun, as these measurements are inherently less precise than abundance determinations from solar twins and analogs. Assuming that these abundances follow a lognormal distribution and that U/Eu is constant throughout the Galaxy ($\text{U}/\text{Eu} = 1/10$), we calculate an average current-day $(\text{Eu}/\text{Mg})_{\text{star}} = (\text{U}/\text{Mg})_{\text{star}} = 0.93$ times the solar ratio (Table A3), with 95% of our sample falling between 0.45 and 1.92 times solar (Figure 1, middle).

Bulk K/Mg ratios show a larger range of variation than Th/Mg and Eu/Mg ratios (Figure 1, right). There are 179 FGK stars with both K and Mg reported in the Hypatia catalog (Hinkel et al. 2014). Assuming that these abundance ratios follow a lognormal distribution, we calculate an average current-day $(\text{K}/\text{Mg})_{\text{star}}$ of 1.13 times the solar ratio (Table A3), with 95% of all data falling between 0.35 and 3.63 times solar (Figure 1, right). Only the single isotope ^{40}K is radioactive, but no data exist for $^{40}\text{K}/\text{K}$ ratios outside of the solar system. For

Figure A7. Same as Figure A6 but for a $6 M_{\oplus}$ planet.

this model setup, a variation in a planet's $^{40}\text{K}/\text{K}$ will effectively act as an increase or decrease in bulk K, similar to our discussion of f_{K} above. We discuss the consequences of the variable volatility of K on our model results in the main text and Appendix B.

By taking our data from the Hypatia catalog, we are implicitly combining abundances from different sources with different measurement uncertainties. Because we adopt the median abundance value if multiple sources are available for the same star, we likely overestimate the range of any abundance ratio in Figure 1.

Our Monte Carlo models described below randomly sample within each distribution of Figure 1 independently. There is observational evidence from solar twins that stellar Th/Eu is roughly constant through Galactic time (Botelho et al. 2019), suggesting that these abundances are correlated. It is not observationally known, however, whether this extends to U/Th in metal-rich stars. Both U and Th are produced via the r -process, and thus their abundances in stars do correlate somewhat. However, ^{40}K is produced via the s -process, and

its correlation with the r -process elements is not known. Bulk K is produced via explosive oxygen burning (Shimansky et al. 2003) and has been observationally shown to correlate with the α -elements (e.g., Mg; Zhang et al. 2006); it is therefore unlikely to correlate with Eu, Th, or U through Galactic time. The models of Frank et al. (2014) capture each of these behaviors; thus, our treatment of $C_X^{\text{planet}}(t)$ somewhat captures the correlation between Eu, U, and Th (Figure A1). Our treatment of the system-to-system variations implied from Figure 1 causes our model to explore some areas of U and Th parameter space that are unlikely. Given that we find these elements to have a minor effect on the longevity of mantle degassing, however, these inclusions of Eu, Th, and U correlations are not likely to substantially change our determinations of Age_{max} .

A.5. Monte Carlo Model

For this work, we adopt a Monte Carlo method for determining the degassing lifetime of planets with a fixed size, CMF, and formation age (in terms of time after Galaxy

formation). In each Monte Carlo suite, $\sim 10^4$ – 10^5 models are run. In each run, C_X^{planet} is determined using Equation (A38) by independently sampling from the lognormal distributions of each HPE as shown in Figure 1 and multiplying by the $C_X^{\text{Earth-like}}$ corresponding to its formation time after the birth of the Milky Way ($t=0$; Figure A1). This method allows us to simulate both the GCE of the HPEs over Galactic history and the system-to-system variation of these HPEs due to their stochastic distribution due to inefficient mixing of these elements throughout the Galaxy.

Unlike the HPE abundances, which can be constrained by stellar observations, other factors that influence a planet’s thermal evolution cannot be constrained observationally. We account for variation in two of the most important of these factors, the initial mantle temperature and mantle reference viscosity, in our models by randomly sampling from uniform distributions across reasonable uncertainty ranges. For the initial mantle temperature, we use a range of 1700–2000 K, and for the mantle reference viscosity, we use a range of 10^{19} – 10^{23} Pa s. The uniform distribution for the reference viscosity is sampled in log space, or, in other words, we sample from a uniform distribution of $\log_{10}(\mu_{\text{ref}}) = 19 - 23$. The range of mantle viscosities considered covers 2 orders of magnitude above and below the typical estimates for the average viscosity of Earth’s mantle based on postglacial rebound studies (e.g., Mitrović & Forte 2004). The initial mantle temperature is not well constrained for Earth or any planet, but our assumed range covers the spread typically used in studies of solar system planets (e.g., Hauck & Phillips 2002; Fraeman & Korenaga 2010; Morschhauser et al. 2011; Breuer & Moore 2015; Foley et al. 2020). With the reference viscosity, initial mantle temperature, and radiogenic heat production rate set, the initial stagnant-lid thickness is calculated assuming that the conductive heat flux at the base of the lid matches the advective heat flux supplied by the convecting mantle. The last remaining parameter to set is the total carbon budget of the mantle and surface reservoirs, C_{tot} .

For our suites of Monte Carlo models, the concentration of CO_2 in the mantle at the model start time is set to $\sim 5 \times 10^{-3}$ wt%, regardless of planet mass or other assumed properties. We examined the effects of higher or lower mantle C contents and found that the lifetime of mantle degassing was insensitive to the total mantle C concentration above $\sim 10^{-5}$ wt%, in agreement with Foley & Smye (2018). Below this threshold, the mantle is more likely to exhaust its entire C budget, causing degassing to end, even if there is a sufficient HPE budget to support volcanism for longer. Above $\sim 10^{-5}$ wt%, there is sufficient mantle CO_2 to support degassing until the planet’s dwindling heat budget no longer supports mantle melting and volcanism. We also assume no CO_2 in the atmosphere at the model start time and, since the models start with no crust present, no CO_2 in the crust either. Whether a planet’s C would initially lie entirely in the mantle (as we assume), the atmosphere, or a combination of the two is not known. However, Foley (2019) found that the initial distribution of C between surface and interior does not significantly affect subsequent climate evolution, at least when liquid water is present and silicate weathering can occur. For an Earth-sized planet, $\approx 5 \times 10^{-3}$ wt% CO_2 scales to a total C budget of 5×10^{21} mol; this value is about a factor of 2 lower than the estimate for the Earth given by Sleep & Zahnle (2001).

Since models are presented in terms of a CO_2 concentration in wt%, larger planets will have larger total C budgets than smaller planets for the same CO_2 concentration. In calculating rates of CO_2 outgassing, our models assume that the concentration of CO_2 in the source region to mantle melts is set by the (time-evolving) bulk mantle CO_2 concentration. We use melt-solid partition coefficients to then calculate the CO_2 concentration in the resulting melt and hence the rate of CO_2 outgassing. In doing so, we implicitly assume that the mantle oxidation state of the planets we model is the same as the present-day Earth. A more reduced mantle would favor production of more reduced gases at the expense of CO_2 and lower the CO_2 outgassing rate (e.g., Tosi et al. 2017). More reduced conditions also reduce the solubility of C species in mantle melt (e.g., Grewal et al. 2020). A more reduced mantle would thus be equivalent to lower mantle CO_2 concentrations in our models.

All parameters varied in our model are shown in Table A1.

Appendix B

Compositional Changes to Age_{max}

B.1. Effects of GCE on Degassing Lifetime

As the Galaxy aged, HPEs were produced via supernova processes, while those already existing decayed. This is all while the nonradioactive rocky planet-building elements were continuously being produced, thus diluting the concentration of HPEs as the Galaxy aged (Figure A1). This, in turn, caused the average Q_0 , and thus degassing lifetimes, to also decrease as the Galaxy aged (Figure A1, middle). The exact makeup of a planet’s HPE budget also affected the degassing lifetimes. Those planets older than ~ 8 Gyr had initial heat budgets composed primarily of ^{235}U . For planets younger than 8 Gyr, ^{40}K instead became the dominant component of its initial HPE budget. The shorter half-life of ^{235}U (704 Myr) compared to ^{40}K (1.25 Gyr) causes older planets to release their internal heat more rapidly. As a result, the oldest, ^{235}U -dominant planets degas for only ~ 1 Gyr longer than the ^{40}K -dominant planets formed at the same time as the Earth, despite having nearly double the Q_0 and five times as much ^{235}U .

These results suggest that as the Galaxy evolves, newer planets may form with a lower HPE budget than older ones (Figure A1). While we do not extrapolate our results into the future, this potential decrease in HPE abundance would cause degassing lifetimes for stagnant-lid exoplanets to also decrease. In order to counteract the decay and subsequent dilution of radionuclides as the Galaxy evolves, the likelihood of a rocky exoplanet supporting a temperate climate may be more reliant on the local emplacement of HPE-rich material from supernova sources to boost its radiogenic heat budget above the average from GCE. Exploring these effects is beyond the scope of this paper, but our results point to the need for more work exploring the spatial and temporal distribution of the long-lived HPEs due to GCE.

B.2. Planetary K Concentration

We first consider possible sources of error or bias in our estimated probability distributions for the mantle abundances of the four major HPEs in rocky exoplanets as derived from stellar chemistry observations. Of the four HPEs we considered, a rocky exoplanet’s mantle concentration of ^{40}K is dependent on both the disk’s bulk abundance of ^{40}K and

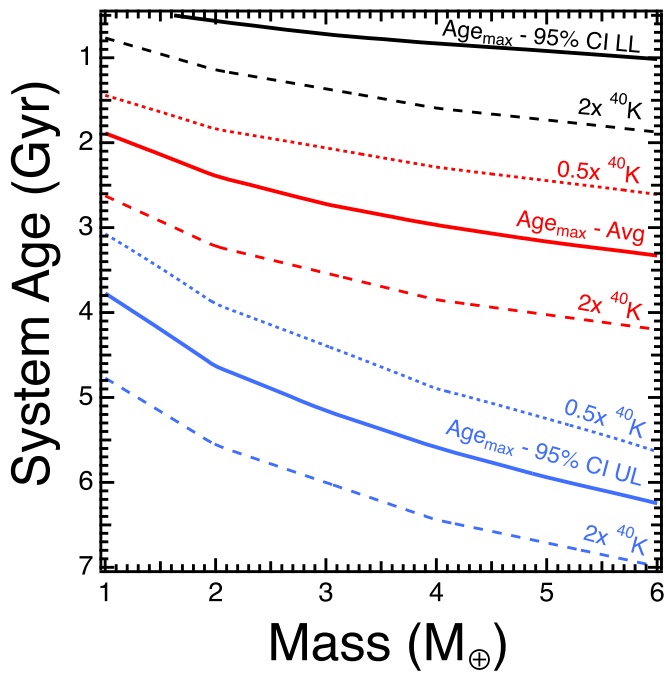


Figure B1. Best-fit average (red) and upper (blue) and lower (black) limits of the 95% confidence interval of Age_{max} assuming that ^{40}K is arbitrarily halved (dotted), left Earth-like (solid), and doubled (dashed) in Equation (A37) for 25,000 model iterations for each curve.

depletion of K relative to the refractory rock-forming elements during planetary formation. Unlike Th and U, K is moderately volatile, meaning that there could be significant differences between the measured stellar abundances and the resulting planetary abundances. In our solar system, accretion of chondrites themselves cannot explain the depletion of K by the factor of 5 seen in Earth relative to the Sun. Moderately volatile elements within chondrules (igneous melt spherules), however, appear to be depleted with respect to the matrix grains by factors comparable to the requisite factor of 5 depletion of K relative to Mg between the Earth and Sun. Perhaps the preferential accretion of chondrules (rather than chondrites) by Earth may explain its depletion (Desch et al. 2020); however, no first-principle models exist that quantitatively predict the degree of depletion of the volatile elements in planetary materials (e.g., see review by Alexander 2005). Whether preferential melting, vaporization, or differentiation play a role in the degree of K volatilization during planet formation is an open but critical question in understanding whether a rocky exoplanet is likely to be temperate today. Until such time as a theory is developed to quantify the range of possible fractionation, all that can be said is that unlike the Th/Mg and U/Mg ratios, the K/Mg ratio of a planet cannot be expected to match its host star, and a volatility/fractionation factor must be assumed for exoplanetary systems. If planets were composed of purely chondritic material, stellar abundances matching planetary abundances might be the case, but based on our solar system, it is more likely that the planet has a lower K/Mg than its host star. This degree of volatilization then remains unknown. Given its effect on the degassing lifetime of rocky exoplanets, work by both the meteoritics and planetary formation communities is critically needed to quantify this parameter in order to better constrain the evolution of rocky exoplanets.

Additionally, the $^{40}\text{K}/\text{K}$ ratio for other stars, and hence planetary systems, is unconstrained. In our previous models, we simply assumed the same depletion factor between the Earth and Sun for all planets and hence the same volatility and $^{40}\text{K}/\text{K}$ ratio as the Earth. However, system-to-system variation in these properties would lead to an even wider distribution of ^{40}K compared to those in Figure 1. The probability of a planet acquiring a larger ^{40}K concentration could therefore be higher than we previously estimated.

To assess how changes in volatility and $^{40}\text{K}/\text{K}$ affect Age_{max} (Figure A5), we reran our models for determining the degassing lifetime as a function of planet formation time and mass (Figure 2) and arbitrarily changed the abundance of ^{40}K (f_x^{K} ; Equation (A37)) by factors of 0.5 and 2. Halving a planet’s ^{40}K abundance decreases $\text{Age}_{\text{max}}^{\text{Avg}}$ by $\sim 500\text{--}700$ Myr and $\text{Age}_{\text{max}}^{\text{UL95\%CI}}$ by $\sim 600\text{--}750$ Myr, with this difference increasing as the mass increases (Figure B1). Doubling the K abundance yields increases in $\text{Age}_{\text{max}}^{\text{Avg}}$ by $\sim 700\text{--}850$ Myr and $\text{Age}_{\text{max}}^{\text{UL95\%CI}}$ by 0.7–1 Gyr. While observations of a host star’s K/Mg abundance can allow us to estimate the degassing lifetime of a rocky exoplanet, differences in the volatilization and/or the system’s $^{40}\text{K}/\text{K}$ abundances compared to Earth will have a direct effect on the location of Age_{max} . Next, we will explore the degree of potential K volatility and the likelihood of systems having non-Earth $^{40}\text{K}/\text{K}$ ratios for comparison to these estimates of ^{40}K -dependent Age_{max} .

B.3. Enrichment of ^{40}K via Supernova Injections and Background Concentration

An efficient method of ^{40}K enrichment might be supernova injection of material into the protoplanetary disk. Supernova remnants frequently exhibit large-scale bipolar or unipolar morphologies (e.g., Leonard et al. 2000; Ouellette et al. 2007; Larsson et al. 2013; Moranchel-Basaruto et al. 2017; Reilly et al. 2017), as well as filaments and clumpy “bullets” of ejected material on smaller scales (e.g., Willingale et al. 2002; Fesen & Milisavljevic 2016; Zhou et al. 2016; García et al. 2017). These sorts of small-scale structures are seen in hydrodynamic simulations (e.g., Hammer et al. 2010; Ellinger et al. 2012; Wongwathanarat et al. 2015). As a result, star- and planet-forming structures near the supernova can be enriched by bullets of material that represent the abundances in a specific part of the explosion, rather than the average yields. This material can be injected as gas into a cloud core or as dust into a protoplanetary disk (Young et al. 2009; Ellinger et al. 2012; Pan et al. 2012). It is possible to estimate the maximum enhancement that such an injection can yield by comparing the amount of ^{40}K in an ejecta clump to the total inventory in the protoplanetary material.

Based on ALMA observations, the dust mass in M dwarf disks is of order $10^{-5} M_{\odot}$, and the total disk mass for a dust-to-gas ratio of 1:100 is $10^{-3} M_{\odot}$ (Ward-Duong et al. 2018). If a $10^{-3} M_{\odot}$ disk initially contains a solar K concentration of 3.7 ppm ($3.7 \mu\text{g K g}^{-1}$ of disk) and the primordial solar $^{40}\text{K}/\text{K}$ (0.14%) of Lodders (2003), the masses of the bulk K and ^{40}K in the disk are 3.7×10^{-9} and $5.17 \times 10^{-12} M_{\odot}$, respectively. For an individual $15 M_{\odot}$ supernova progenitor (Figure B2; Ellinger et al. 2012), we calculate a peak mass fraction of bulk K and ^{40}K potentially injected into the disk of $\sim 10^{-3.6}$ and $\sim 10^{-4.7}$, respectively (Figure B3). This corresponds to $^{40}\text{K}/\text{K} \sim 10^{-1.1}$ (8%). The average mass of a bullet in our model is $10^{-5} M_{\odot}$. For a $10^{-5} M_{\odot}$ bullet mass, then, we estimate that

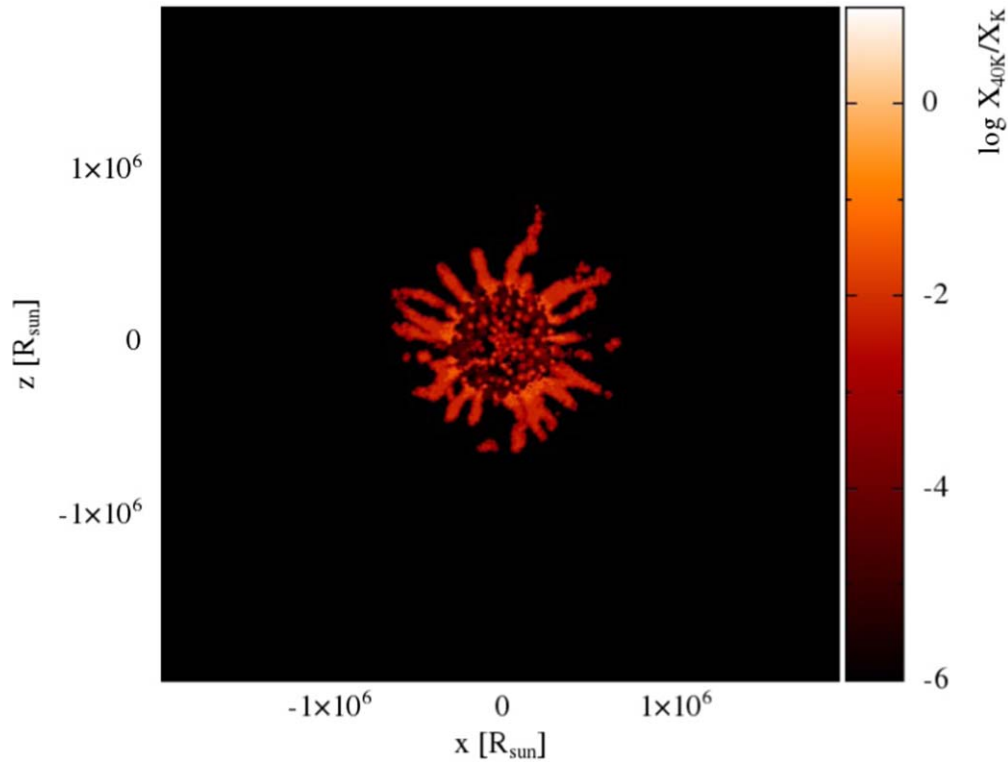


Figure B2. Cross section of ejecta in a mildly bipolar explosion of a $15 M_{\odot}$ star. Axes are in units of solar radii. The color bar represents the log of the mass ratio of ^{40}K to total K. The peak $^{40}\text{K}/\text{K}_{\text{tot}}$ occurs in areas of large overdensity near the base of the Rayleigh–Taylor fingers. These clumps persist out to large radii during the remnant phase of the supernova.

$\sim 2.5 \times 10^{-11} M_{\odot}$ of K and $2 \times 10^{-12} M_{\odot}$ of ^{40}K are delivered to the disk via the injection of supernova material. Injecting a single $10^{-5} M_{\odot}$ bullet into our disk raises the total mass of K in the disk by $<1\%$ and ^{40}K by $\sim 39\%$. This would raise the disk’s primordial $^{40}\text{K}/\text{K}$ to $\sim 0.19\%$. The injection of this super-enriched supernova-derived ^{40}K material will account for an increase in the protoplanetary disk’s $^{40}\text{K}/\text{K}$ by only $\sim 36\%$.

As the disk mass increases above $10^{-3} M_{\odot}$, the relative mass contribution of high- $^{40}\text{K}/\text{K}$ material from these injections to the protoplanetary disk begins to diminish. For the minimum-mass solar nebula of $0.013 M_{\oplus}$ (Hayashi 1981; Kuchner 2004), the contribution from a single injection increases the disk’s $^{40}\text{K}/\text{K}$ by $<1\%$. Thus, while $^{40}\text{K}/\text{K}$ can increase somewhat due to the direct injection of supernova material, this mechanism is likely to only affect the radiogenic heat budgets of planets forming in low-mass, M dwarf disks, and only marginally, leading only to a <500 Myr increase in Age_{max} (Figure B3). Larger bullet masses on the order of $10^{-4} M_{\odot}$, however, are possible (Young et al. 2009; Ellinger et al. 2012), which would allow for a significant enrichment for higher-mass disks. The relative occurrence rates of these high-mass bullets are unconstrained and beyond the scope of this paper. Thus, we offer only a conservative estimate of ^{40}K enrichment via supernova injection. We argue then that supernova events are not likely to increase a planet’s radiogenic heat budget and degassing lifetime enough to drastically change Age_{max} for all but those planets orbiting low-mass stars. Instead, a system’s bulk K abundance and the degree of K volatilization are the most likely first-order sources for increasing a rocky exoplanet’s radiogenic heat budget and degassing lifetime. In this sense then, observations of the host star’s K/Mg coupled with modeling of the range of volatility are the most likely avenues

for quantifying whether a planet contains sufficient K to be actively degassing today.

B.4. Mantle Water Content

We estimate how increasing the mantle water content would influence Age_{Max} , taking into account the competing effects of water content on mantle viscosity and solidus. Viscosity has been found to scale as $(1/\chi_m)^r$, where χ_m is the mantle water concentration, expressed here as the water mass fraction, and r is an experimentally determined exponent, $r = 0.7\text{--}1.2$, according to the compilation in Hirth & Kohlstedt (2003). Drier mantles would thus have higher viscosities, up to a point (there is a threshold water content where the material is effectively dry, and further decreases in water content will not affect viscosity), and wetter mantles would have lower viscosities. At the same time, water content also affects the mantle solidus, with melting temperatures decreasing as mantle water content increases (e.g., Kushiro et al. 1968). These two effects counteract each other: a drier mantle has a higher viscosity, acting to extend the degassing lifetime and Age_{max} , but also a higher solidus temperature, which inhibits melting and acts to lower the degassing lifetime and Age_{max} .

Ultimately, to fully capture these competing effects, new models incorporating the combined effects of water on viscosity and solidus, and how mantle water content evolves over time due to in- and outgassing from the mantle (e.g., McGovern & Schubert 1989; Crowley et al. 2011; Spaargaren et al. 2020), would be needed. However, we can provide a first-order estimate using two additional model suites where the solidus temperature is first lowered by 100 K everywhere, then by 200 K, and the mantle reference viscosity is systematically varied as before. From the results of these model suites, we find

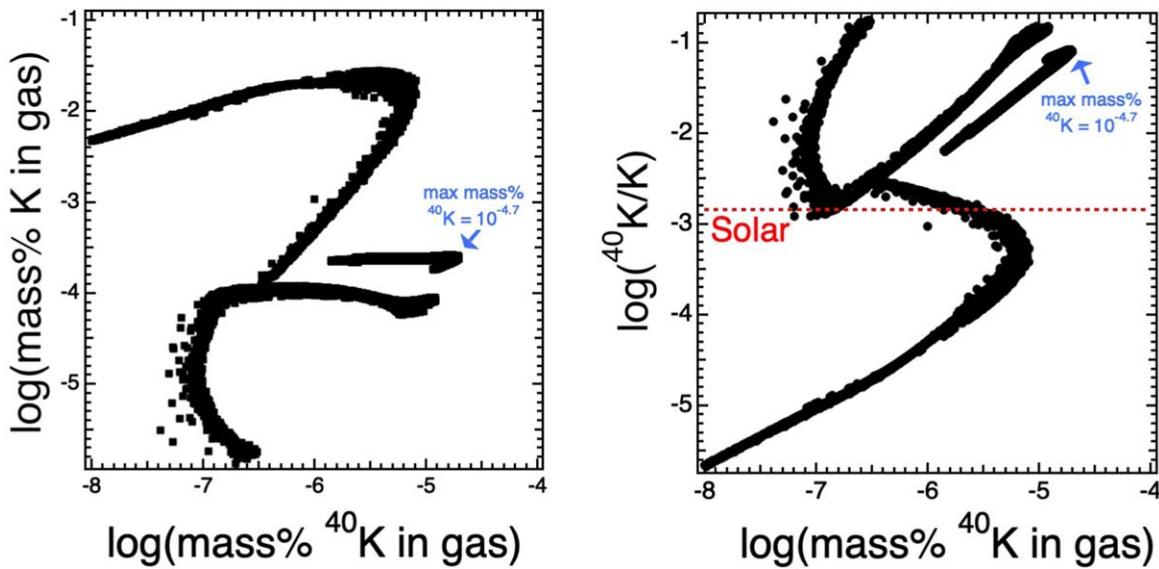


Figure B3. Left: mass percentage of bulk K and ^{40}K in the gas for a $15 M_{\odot}$ progenitor. Right: $^{40}\text{K}/\text{K}$ vs. mass fraction of ^{40}K in the gas for the same progenitor (Ellinger et al. 2012). The Sun’s primordial $^{40}\text{K}/\text{K}$ is shown for reference (Lodders 2003).

that, on average, the degassing lifetime increases by ≈ 0.43 Gyr per 100 K decrease in solidus temperature for a $1 M_{\oplus}$ planet and ≈ 0.60 Gyr for $6 M_{\oplus}$ (Figure B4). We then use the diffusion creep viscosity flow laws from Hirth & Kohlstedt (2003) and the solidus parameterization from Katz et al. (2003) to estimate how Age_{max} would change with increasing water content. We start from the water content where the wet viscosity flow law is equal to the dry viscosity flow law and increase the water content from this point up to ≈ 0.3 wt% (Figure B5). For comparison, the Earth’s mantle water content is estimated to be 10^{-2} wt% (Ohtani 2019). We do this for a range of water viscosity dependency exponents, r .

For both 1 and $6 M_{\oplus}$ planets, increasing the water content first decreases $\text{Age}_{\text{Max}}^{\text{Avg}}$ in comparison to a dry-planet baseline. Here the effect of decreasing the mantle reference viscosity due to a higher water content dominates because the solidus temperature does not decrease significantly from that of dry peridotite until the water content approaches ≈ 0.05 – 0.1 wt%. When the water content increases beyond this point ($\chi_m \gtrsim 0.05$ – 0.1 wt%), the decrease in solidus temperature begins to dominate over the decrease in viscosity, and the change in Age_{max} compared to a dry-planet baseline begins to increase. The higher the r , the more the viscosity effect dominates, as mantle viscosity is more sensitive to water content in this case. For a $1 M_{\oplus}$ planet, $\text{Age}_{\text{Max}}^{\text{Avg}}$ could decrease by up to ≈ 1.4 Gyr when $\chi_m = 0.05$ wt% and $r = 1.2$. Meanwhile, $\text{Age}_{\text{Max}}^{\text{Avg}}$ could increase by up to ≈ 1.6 Gyr for $\chi_m = 0.3$ wt% and $r = 0.7$. The effects are larger for a $6 M_{\oplus}$ planet, with the biggest decrease in $\text{Age}_{\text{Max}}^{\text{Avg}}$ being ≈ 2.1 Gyr and the biggest increase being ≈ 2.3 Gyr. Note again that these estimates assume fixed mantle water concentrations, when in reality, the water concentration would evolve over time as a result of in- and outgassing. On a stagnant-lid planet, ingassing will be limited (e.g., Spaargaren et al. 2020), so the mantle water content is likely to decrease over time; this means the changes to Age_{max} presented here are likely upper limits.

Mantle water content, then, is an important parameter that can have a large effect on Age_{max} . Should a planet’s mantle form with an Earth-like concentration (10^{-2} wt%), $\text{Age}_{\text{Max}}^{\text{Avg}}$ is

roughly the same as or lower than the dry mantle model (Figure A5). It is only those planets with mantles enriched in water relative to the Earth by a factor of 10–100 where $\text{Age}_{\text{Max}}^{\text{Avg}}$ increases, according to our simple estimates. Planets forming with this much water is a possibility (e.g., Raymond et al. 2004; Unterborn et al. 2018). However, despite a lower mantle solidus promoting melting on such water-rich planets, there are other factors that could hamper their habitability and the possibility of detecting biosignatures on such planets, should they be inhabited. Exposed land may be essential for life on Earth, as weathering of subaerial land supplies critical nutrients to the oceans (e.g., Maruyama et al. 2013; Dohm & Maruyama 2015), and some leading theories for the origin of life rely on wet–dry cycles and therefore require exposed land (e.g., Bada & Korenaga 2018). For an Earth-mass planet, complete flooding of the surface is expected to occur when the mass of surface water is roughly that of 8–40 oceans. This equates to $\sim 0.2\%$ of the mass of the planet, with this mass-fraction threshold decreasing with increasing planet mass due to higher gravity limiting surface topography (Kite et al. 2009; Cowan & Abbot 2014).

Furthermore, as the surface water content increases, the pressure at the water–rock interface increases, forcing melting to occur at higher temperatures, limiting mantle degassing (Kite et al. 2009; Cowan & Abbot 2014). This pressure effect would then counteract the effect of mantle water content on the solidus temperature and therefore potentially limit the increase in Age_{max} at higher mantle water concentrations than in Figure B5 (where ocean bottom pressure is assumed to be negligible for mantle melting). In fact, for a very thick ocean layer, pressures may be high enough to shut down degassing entirely (Kite et al. 2009; Krissansen-Totton et al. 2021) by preventing melting or forcing melting to occur at such high pressures that the melt would no longer be buoyant. Moreover, even if life were to develop on an ocean-covered planet with mantle degassing, the detectability of life on these planets is more difficult (Glaser et al. 2020). This is because, for planets with enough surface water to submerge the continental crust, the weathering rate of the biocritical element phosphorus is

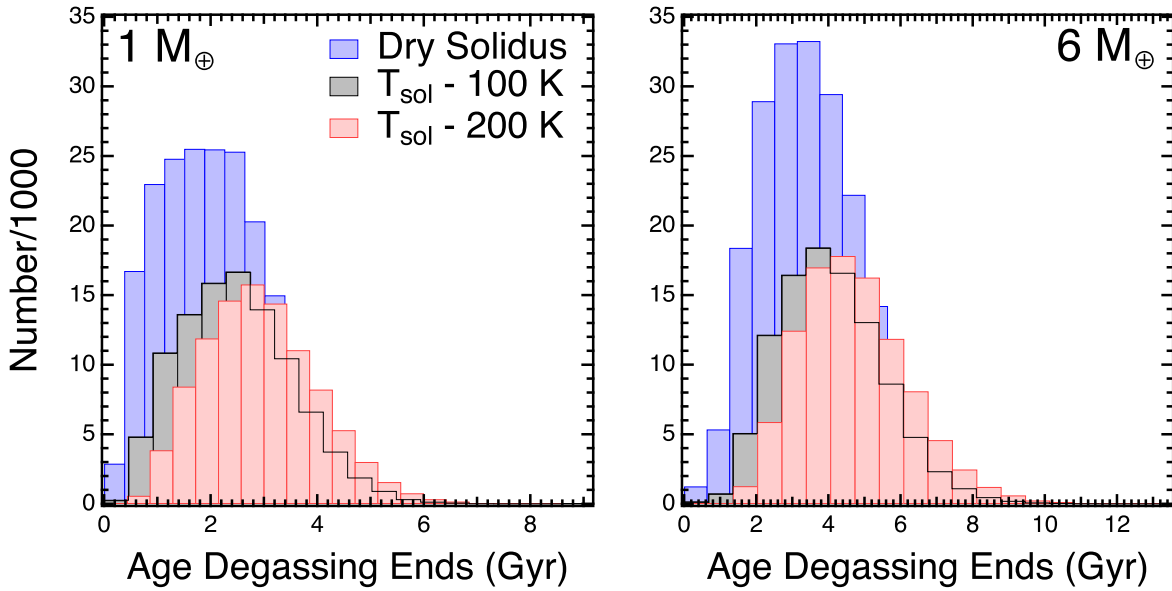


Figure B4. Histograms of the age when planetary degassing ends for 1 (left) and 6 (right) M_{\oplus} planets with our default solidus (blue) and the solidus decreased arbitrarily by 100 (gray) and 200 (red) Kelvin. These histograms represent 200,000 random samplings of our parameters as described in Appendix A.5.

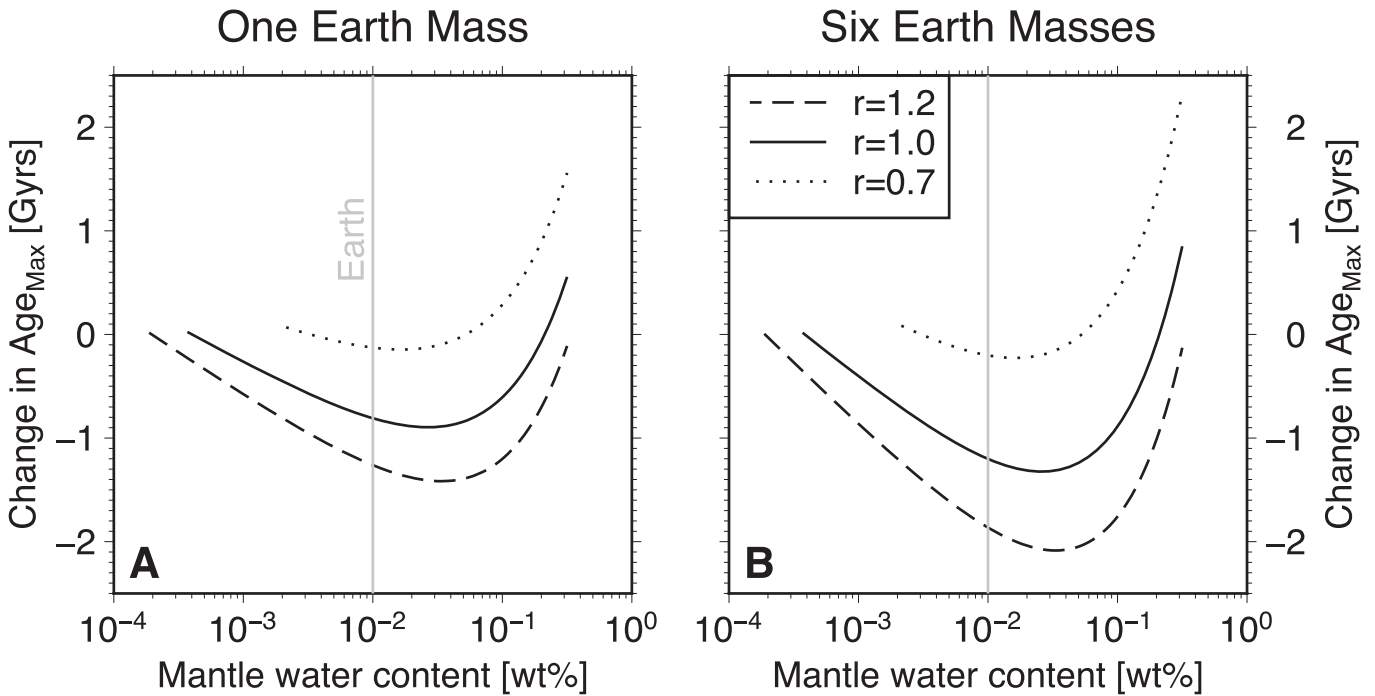


Figure B5. Change in $\text{Age}_{\text{Max}}^{\text{Avg}}$ in comparison to a dry-planet baseline as a function of mantle water content. Three different values of the viscosity water dependence exponent, r , are used: $r = 0.7$ (dotted line), 1 (solid line), and 1.2 (dashed line). Results for 1 (a) and 6 (b) M_{\oplus} are presented. The lower bound on the mantle water concentration for each curve is determined by the mantle water concentration where the dry and wet olivine flow laws are equal. This crossover point depends on r , which is why curves with different r do not start at the same point in terms of mantle water concentration. The vertical gray line denotes Earth’s mantle’s estimated water content.

significantly reduced. With less bioavailable P, the biogenic flux of O_2 is reduced, becoming comparable to the abiotic O_2 flux (Glaser et al. 2020). Even for those water worlds where the pressure at the water–mantle boundary allows for mantle degassing, as these planets age, degassing will wane. In this case, the source of reductants from the mantle will also decrease, allowing abiotic O_2 to build up in the atmosphere, potentially masking any biotic source of O_2 (Krissansen-Totton et al. 2021). Each of these factors will limit our ability to

distinguish between biotic or abiotic O_2 through atmospheric observations, even though the planet may be habitable and hosting life.

Therefore, it is unclear whether high water concentrations ($\gtrsim 0.2$ wt%) would actually promote long-lived mantle degassing, temperate climates, and habitability. Instead, for water contents $\lesssim 0.2$ wt%, where continents may still be exposed on small exoplanets, increasing water content generally leads to lower degassing lifetimes and a lower

Age_{max}. While more work is needed to quantify these differences as a function of planet mass, our results shown in Figure A5 may represent the most optimistic case for Age_{max} with regard to mantle water content.

ORCID iDs

Cayman T. Unterborn  <https://orcid.org/0000-0001-8991-3110>

Bradford J. Foley  <https://orcid.org/0000-0002-6943-3192>

Steven J. Desch  <https://orcid.org/0000-0002-1571-0836>

Patrick A. Young  <https://orcid.org/0000-0003-1705-5991>

Stephen R. Kane  <https://orcid.org/0000-0002-7084-0529>

References

- Abbot, D. S., Cowan, N. B., & Ciesla, F. J. 2012, *ApJ*, 756, 178
- Agol, E., Dorn, C., Grimm, S. L., et al. 2021, *PSJ*, 2, 1
- Akeson, R. L., Chen, X., Ciardi, D., et al. 2013, *PASP*, 125, 989
- Alexander, C. M. O. 2005, *M&PS*, 40, 943
- Bada, J. L., & Korenaga, J. 2018, *Life*, 55, 8(4)
- Ballmer, M. D., Houser, C., Hermlund, J. W., Wentzcovitch, R. M., & Hirose, K. 2017, *NatGe*, 10, 236
- Barbuy, B., Spite, M., Hill, V., et al. 2011, *A&A*, 534, A60
- Barnes, R., Jackson, B., Raymond, S., West, A., & Greenberg, R. 2009, *ApJ*, 695, 1006
- Beattie, P. 1993, *Natur*, 363, 63
- Beers, T. C., & Christlieb, N. 2005, *ARA&A*, 43, 531
- Bercovici, D., Tackley, P., & Ricard, Y. 2015, in *Treatise on Geophysics, Mantle Dynamics*, ed. D. Bercovici & G. Schubert (New York: Elsevier)
- Borrelli, M. E., O'Rourke, J. G., Smrekar, S. E., & Ostberg, C. M. 2021, *JGRE*, 126, e06756
- Botelho, R. B., Milone, A. d. C., Meléndez, J., et al. 2019, *MNRAS*, 482, 1690
- Breuer, D., & Moore, W. 2015, in *Treatise on Geophysics (Second Edition)*, ed. G. Schubert (Oxford: Elsevier), 255
- Burgasser, A. J., & Mamajek, E. E. 2017, *ApJ*, 845, 110
- Byrne, P. K., Ghail, R. C., Celâl Şengör, A. M., et al. 2021, *PNAS*, 118, 2025919118
- Byrne, P. K., & Krishnamoorthy, S. 2022, *JGRE*, 127, e2021JE007040
- Cowan, N. B., & Abbot, D. S. 2014, *ApJ*, 781, 27
- Crisp, J. A. 1984, *JVGR*, 20, 177
- Crowley, J. W., G erault, M., & O'Connell, R. J. 2011, *EPSL*, 310, 380
- Davaille, A., Smrekar, S. E., & Tomlinson, S. 2017, *NatGe*, 10, 349
- Desch, S. J., Abbot, D., Krijt, S., et al. 2020, *Planetary Diversity (Bristol: IOP Publishing)*
- Desch, S. J., Kalyaan, A., & Alexander, C. M. O. 2018, *ApJS*, 238, 11
- Dohm, J. M., & Maruyama, S. 2015, *Geosci. Front.*, 6, 95
- Dorn, C., Noack, L., & Rozel, A. B. 2018, *A&A*, 614, A18
- Driscoll, P., & Bercovici, D. 2014, *PEPI*, 236, 36
- Driscoll, P. E., & Barnes, R. 2015, *AsBio*, 15, 739
- Duffy, T., Madhusudhan, N., & Lee, K. 2015, in *Treatise on Geophysics (Second Edition)*, ed. G. Schubert (Oxford: Elsevier)
- Ellinger, C. I., Young, P. A., Fryer, C. L., & Rockefeller, G. 2012, *ApJ*, 755, 160
- Fegley, B., & Prinn, R. G. 1989, *Natur*, 337, 55
- Fesen, R. A., & Milisavljevic, D. 2016, *ApJ*, 818, 17
- Filiberto, J., Trang, D., Treiman, A. H., & Gilmore, M. S. 2020, *SciA*, 6, eaax7445
- Foley, B. J. 2019, *ApJ*, 875, 72
- Foley, B. J., Bercovici, D., & Landuyt, W. 2012, *E&PSL*, 331, 281
- Foley, B. J., & Driscoll, P. E. 2016, *GGG*, 17, 1885
- Foley, B. J., Houser, C., Noack, L., & Tosi, N. 2020, in *Planetary Diversity: Rocky Planet Processes and their Observational Signatures*, ed. E. J. Tasker (Bristol: IOP Publishing)
- Foley, B. J., & Smye, A. J. 2018, *AsBio*, 18, 873
- Fraeman, A. A., & Korenaga, J. 2010, *Icar*, 210, 43
- Frank, E. A., Meyer, B. S., & Mojzsis, S. J. 2014, *Icar*, 243, 274
- Frebel, A., Christlieb, N., Norris, J. E., et al. 2007, *ApJL*, 660, L117
- García, F., Suárez, A. E., Miceli, M., et al. 2017, *A&A*, 604, L5
- Glaser, D. M., Hartnett, H. E., Desch, S. J., et al. 2020, *ApJ*, 893, 163
- Goriely, S., & Arnould, M. 2001, *A&A*, 379, 1113
- Grewal, D. S., Dasgupta, R., & Farnell, A. 2020, *GeCoA*, 280, 281
- G lcher, A. J. P., Gerya, T. V., Mont esi, L. G. J., & Munch, J. 2020, *NatGe*, 13, 547
- Hammer, N. J., Janka, H. T., & M ller, E. 2010, *ApJ*, 714, 1371
- Hansen, T. T., Simon, J. D., Marshall, J. L., et al. 2017, *ApJ*, 838, 44
- Haqq-Misra, J., Koppalapu, R. K., Batalha, N. E., Harman, C. E., & Kasting, J. F. 2016, *ApJ*, 827, 120
- Hart, S. E., & Brooks, C. 1974, *GeCoA*, 38, 1799
- Hauck, S. A., & Phillips, R. J. 2002, *JGRE*, 107, 6
- Hauri, E. H., Gaetani, G. A., & Green, T. H. 2006, *E&PSL*, 248, 715
- Hayashi, C. 1981, *PTHPS*, 70, 35
- Hayworth, B. P. C., & Foley, B. J. 2020, *ApJL*, 902, L10
- Hinkel, N. R., Timmes, F., Young, P. A., Pagano, M. D., & Turnbull, M. C. 2014, *AJ*, 148, 54
- Hinkel, N. R., & Unterborn, C. T. 2018, *ApJ*, 853, 83
- Hirose, K., Labrosse, S., & Hermlund, J. 2013, *AREPS*, 41, 657
- Hirth, G., & Kohlstedt, D. 1996, *E&PSL*, 144, 93
- Hirth, G., & Kohlstedt, D. 2003, in *Subduction Factory Mongraph*, ed. J. Eiler (Washington, DC: Am. Geophys. Union), 83
- Kadoya, S., & Tajika, E. 2014, *ApJ*, 790, 107
- Karato, S. 2011, *Icar*, 212, 14
- Karato, S., & Wu, P. 1993, *Sci*, 260, 771
- Kasting, J. F., & Catling, D. 2003, *ARA&A*, 41, 429
- Kasting, J. F., Whitmire, D. P., & Reynolds, R. T. 1993, *Icar*, 101, 108
- Katz, R. F., Spiegelman, M., & Langmuir, C. H. 2003, *GGG*, 4, 1073
- Kislyakova, K. G., Noack, L., Johnstone, C. P., et al. 2017, *NatAs*, 1, 878
- Kite, E. S., & Ford, E. B. 2018, *ApJ*, 864, 75
- Kite, E. S., Manga, M., & Gaidos, E. 2009, *ApJ*, 700, 1732
- Koppalapu, R. K., Ramirez, R., Kasting, J. F., et al. 2013, *ApJ*, 765, 131
- Korenaga, J. 2009, *GeoJ*, 179, 154
- Krissansen-Totton, J., & Catling, D. C. 2017, *NatCo*, 8, 15423
- Krissansen-Totton, J., Galloway, M. L., Wogan, N., Dhaliwal, J. K., & Fortney, J. J. 2021, *ApJ*, 913, 107
- Kuchner, M. J. 2004, *ApJ*, 612, 1147
- Kushiro, I., Syono, Y., & Akimoto, S. 1968, *JGR*, 73, 6023
- Larsson, J., Fransson, C., Kjaer, K., et al. 2013, *ApJ*, 768, 89
- Leonard, D. C., Filippenko, A. V., Barth, A. J., & Matheson, T. 2000, *ApJ*, 536, 239
- Lodders, K. 2003, *ApJ*, 591, 1220
- Lodders, K., Palme, H., & Gail, H. P. 2009, 4.4 Abundances of the elements in the Solar System (Berlin: Springer), 712
- Marty, B., & Tolstikhin, I. N. 1998, *ChGeo*, 145, 233
- Maruyama, S., Ikoma, M., Genda, H., et al. 2013, *Geosci. Front.*, 4, 141
- McDonough, W. F. 2003, in *Treatise on Geochemistry, Volume 2*, ed. R. W. Carlson (Amsterdam: Elsevier), 547
- McGovern, P., & Schubert, G. 1989, *E&PSL*, 96, 27
- Menou, K. 2015, *E&PSL*, 429, 20
- Mitrovica, J. X., & Forte, A. M. 2004, *E&PSL*, 225, 177
- Moranchel-Basurto, A., Vel zquez, P. F., Giacani, E., et al. 2017, *MNRAS*, 472, 2117
- Morschhauser, A., Grott, M., & Breuer, D. 2011, *Icar*, 212, 541
- Nimmo, F., Primack, J., Faber, S. M., Ramirez-Ruiz, E., & Safarzadeh, M. 2020, *ApJL*, 903, L37
- Noack, L., & Breuer, D. 2014, *P&SS*, 98, 41
- Noack, L., H ning, D., Rivoldini, A., et al. 2016, *Icar*, 277, 215
- Ohtani, E. 2019, *Natl. Sci. Rev.*, 7, 224
- O'Neill, C., & Lenardic, A. 2007, *Geochim. Cosmochim. Acta*, 71, 19204
- Oosterloo, M., H ning, D., Kamp, I. E. E., & van der Tak, F. F. S. 2021, *A&A*, 649, A15
- O'Rourke, J. G., & Korenaga, J. 2015, *Icar*, 260, 128
- Ouellette, N., Desch, S. J., & Hester, J. J. 2007, *ApJ*, 662, 1268
- Palme, H., & O'Neill, H. S. C. 2003, *TrGeo*, 2, 1
- Pan, L., Desch, S. J., Scannapieco, E., & Timmes, F. X. 2012, *ApJ*, 756, 102
- Raymond, S. N., Quinn, T., & Lunine, J. I. 2004, *Icar*, 168, 1
- Reese, C. C., Solomatov, V. S., & Moresi, L.-N. 1998, *JGR*, 103, 13643
- Reese, C. C., Solomatov, V. S., & Moresi, L.-N. 1999, *Icar*, 139, 67
- Reese, C. C., Solomatov, V. S., & Orth, C. P. 2007, *JGRE*, 112, E04S04
- Reilly, E., Maund, J. R., Baade, D., et al. 2017, *MNRAS*, 470, 1491
- Roederer, I. U., Kratz, K.-L., Frebel, A., et al. 2009, *ApJ*, 698, 1963
- Sandwell, D. T., & Schubert, G. 1992, *Sci*, 257, 766
- Schaefer, L., & Sasselov, D. 2015, *ApJ*, 801, 40
- Schubert, G., Cassen, P., & Young, R. E. 1979, *Icar*, 38, 192
- Schulze, J. G., Wang, J., Johnson, J. A., et al. 2021, *PSJ*, 2, 113
- Shen, Y., Solomon, S. C., Bjarnason, I. T., & Wolfe, C. J. 1998, *Natur*, 395, 62
- Shimansky, V. V., Bikmaev, I. F., Galeev, A. I., et al. 2003, *ARep*, 47, 750

- Sleep, N., & Zahnle, K. 2001, *JGR*, **106**, 1373
- Sleep, N. H., & Zahnle, K. 2001, *JGR*, **106**, 1373
- Smrekar, S. E., Stofan, E. R., Mueller, N., et al. 2010, *Sci*, **328**, 605
- Solomatov, V. S., & Moresi, L.-N. 2000, *JGR*, **105**, 21795
- Spaargaren, R. J., Ballmer, M. D., Bower, D. J., Dorn, C., & Tackley, P. J. 2020, *A&A*, **643**, A44
- Spohn, T. 1991, *Icar*, **90**, 222
- Stamenkovic, V., Breuer, D., & Spohn, T. 2011, *Icar*, **216**, 572
- Stevenson, D. J., Spohn, T., & Schubert, G. 1983, *Icar*, **54**, 466
- Tackley, P. J., Ammann, M., Brodholt, J. P., Dobson, D. P., & Valencia, D. 2013, *Icar*, **225**, 50
- Takahashi, E., & Kushiro, I. 1983, *AmMin*, **68**, 859, https://pubs.geoscienceworld.org/msa/ammin/article/68/9-10/859/41545/Melting-of-a-dry-peridotite-at-high-pressures-and?casa_token=jAY2wvw1C88AAAAA:77aTDhMo-nSmSB9xjqLpRpJTXkAyXMLJ_ZVTR9Am_A9y-ZE1RXIEvo94ZA35UQxHOU2U-bw0A
- Taylor, S., & McLennan, S. 1985, *The Continental Crust: Its Composition and Evolution* (Oxford: Blackwell), 312, <https://www.osti.gov/biblio/6582885>
- Thompson, R. N., & Gibson, S. A. 2000, *Natur*, **407**, 502
- Tosi, N., Godolt, M., Stracke, B., et al. 2017, *A&A*, **605**, A71
- Turcotte, D., & Schubert, G. 2002, *Geodynamics* (Second Edition) (New York: Cambridge Univ. Press)
- Unterborn, C. T., Desch, S. J., Hinkel, N. R., & Lorenzo, A. 2018, *NatAs*, **2**, 297
- Unterborn, C. T., Johnson, J. A., & Panero, W. R. 2015, *ApJ*, **806**, 139
- Unterborn, C. T., & Panero, W. R. 2019, *JGRE*, **124**, 1704
- Valencia, D., O'Connell, R. J., & Sasselov, D. 2006, *Icar*, **181**, 545
- Valencia, D., O'Connell, R. J., & Sasselov, D. D. 2007, *ApJL*, **670**, L45
- van Heck, H. J., & Tackley, P. J. 2011, *E&PSL*, **310**, 252
- Walker, J., Hayes, P., & Kasting, J. 1981, *JGR*, **86**, 9776
- Ward-Duong, K., Patience, J., Bulger, J., et al. 2018, *AJ*, **155**, 54
- Warren, J. M. 2016, *Litho*, **248**, 193
- Wasson, J. T., Kallemeyn, G. W., Runcorn, S. K., Turner, G., & Woolfson, M. M. 1988, *RSPTA*, **325**, 535
- White, R. S., & McKenzie, D. 1995, *JGR*, **100**, 17
- Willingale, R., Bleeker, J. A. M., van der Heyden, K. J., Kaastra, J. S., & Vink, J. 2002, *A&A*, **381**, 1039
- Wongwathanarat, A., Müller, E., & Janka, H. T. 2015, *A&A*, **577**, A48
- Young, P. A., Ellinger, C. I., Arnett, D., Fryer, C. L., & Rockefeller, G. 2009, *ApJ*, **699**, 938
- Zhang, H. W., Gehren, T., Butler, K., Shi, J. R., & Zhao, G. 2006, *A&A*, **457**, 645
- Zhao, Y.-H., Zimmerman, M. E., & Kohlstedt, D. L. 2009, *E&PSL*, **287**, 229
- Zhou, P., Chen, Y., Safi-Harb, S., et al. 2016, *ApJ*, **831**, 192